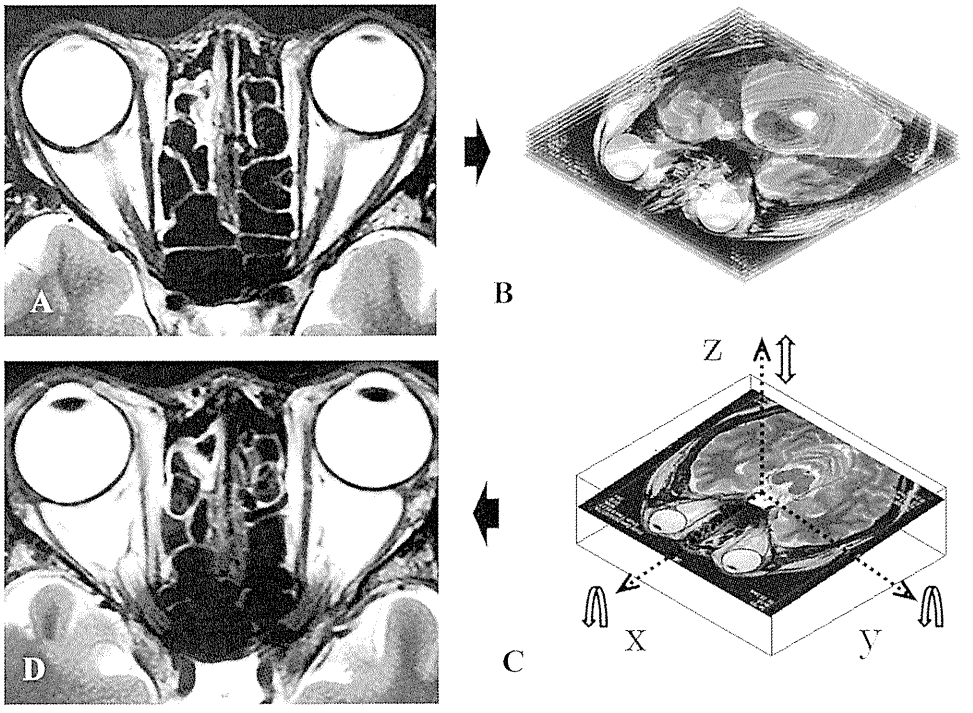

FIGURE 1. (A) In the unprocessed MRI, it was confirmed that the bilateral lenses, optic nerves, medial and lateral rectus muscles, and optic chiasm were depicted clearly in the horizontal images. (B) A 3D restructuring of the head MRIs from the horizontal MRI of a 3-mm slice. (C) To adjust the working reference plane, the optic chiasm of the unprocessed MRI was set to the intersection graph. The *y*-axis was set in parallel with both eyeballs. In addition, the *x*-axis was set orthogonal to the *y*-axis. The *z*-axis was vertically set as the working reference plane, orthogonal to the *x*- and *y*-axes. The *x*-axis was rotated to create a shape that ensured that the crystalline lenses of both eyes appeared the same. Then the *y*-axis was rotated so that the anterior chamber is at its greatest depth. Finally, the z-axis was moved up and down so that the crystalline lens might attain its maximum size; (D) A restructured horizontal MRI of patient 4 (Table 1, 73 years, female).

refractive error of seven subjects without ocular or intracranial diseases were measured for MRI validation.

MRIs were obtained with a 1.5-Tesla superconducting magnet (Gyroscan Intera and Gyroscan Power Trak 1000; Philips Medical Systems, Best, The Netherlands) with a phased-array head coil. Horizontal T_1- and T_2-weighted images were obtained for all patients. T_2-weighted images were obtained using the fast spin-echo method, with a pixel bandwidth of 100 to 150 kH, repetition time (TR) of 2500 to 2948 ms, echo time (TE) of 90 to 130 ms, section thickness of 1.2 to 3 mm, field of view of 70 × 70- to 95 × 95-mm, image frequency of 63.9, pixel spacing of 0.429 to 0.625 pixel/mm, flip angle of 90°, and an acquisition matrix of 256 × 256 to 320 × 320. T_1-weighted images were obtained with a spin-echo sequence with a TR of 480 to 574 ms, TE of 14 to 18 ms, section thickness of 1.2 to 3 mm, image frequency of 63.9, pixel spacing of 0.313 to 0.429 pixel/mm, and flip angle of 90°.

All patients were imaged while supine, and those aged 6 years or younger were sedated. All ocular dimension measurements were made from the horizontal images at approximately 16 magnifications on a computer monitor with a standard resolution of 512 × 512 pixels. The distances were measured with a line caliper in a software program, and the distance between the two points was converted from pixels to millimeters by using pixel-spacing data. Axial length (AL) and width of the right eye were measured from the horizontal MRIs. As the T_2-weighted images were used to apply EFDs, the shaft length of the inside of the eyeball was measured in the AL measurements. AL was recorded as the distance between the posterior cornea and the approximate location of the fovea along the line that bisected the eye in the horizontal plane. The eye width was measured between the retinal surfaces on either side across the horizontal image at the point that visually appeared the widest.

MRI Validation

As our examinations were part of a retrospective study and the MRIs of the infants in that study were taken with the subjects under sedation, it was not possible to fix the visual line on these images. Therefore, a

TABLE 1. A Comparison of Axial Lengths Determined by MRI and A-scan Ultrasonography

Participant Age, Sex	Eye	Mean SER (D)	A-scan US AL (mm)	MRI-AL (mm)	3D-AL (mm)	(A-scan US AL) Minus (MRI-AL)	(A-scan US AL) Minus (3D-AL)
56, female	Right	−0.75	23.53	23.31	23.5	0.22	0.03
	Left	−0.5	23.39	23.08	23.5	0.31	−0.11
73, male	Right	−1.25	25.31	24.41	24.8	0.9	0.51
	Left	−0.75	25.21	24.8	25	0.41	0.21
63, female	Right	0.5	22.9	22.86	22.9	0.04	0
	Left	0.75	22.83	22.64	23.1	0.19	−0.27
73, female	Right	−2.5	23.84	23.2	23.7	0.64	0.14
	Left	−1.75	23.57	22.9	23.6	0.67	−0.03
72, male	Right	−1.5	23.39	23.18	23.3	0.21	0.09
	Left	−1.75	23.57	23.43	23.1	0.14	0.47
30, male	Right	−2.25	25.31	25.48	25.1	−0.17	0.21
	Left	−2.00	25.21	24.96	25.6	0.25	−0.39
62, female	Right	0.75	22.95	22.87	22.9	0.08	0.05
	Left	0.25	23.12	22.65	22.9	0.47	0.22
Mean ± SD			23.87 ± 0.96	23.56 ± 0.94	23.79 ± 0.93	0.31 ± 0.28	0.08 ± 0.25

A-scan US, A-scan ultrasonography; 3D, the three-dimensional restructured image.

technique using three-dimensional (3D) MRIs of the eyeball was used to obtain the horizontal MRIs of the eyeball in all analyses at an equal height. We used the unprocessed horizontal MRIs from approximately 7 to 15 unprocessed slices to make the 3D MRI of the eyeball (Figs. 1A, 1B). The x-, y-, and z-axes of these 3D images have been adjusted respectively (ZedView software program; Lexi Corp., Tokyo, Japan), as shown in Figure 1.

The initial experiments confirmed that the bilateral lenses, optic nerves, medial and lateral rectus muscles, and optic chiasm were depicted clearly in the unprocessed horizontal MRIs. In addition, a slice was made in the working reference plane of the rotation. The center of the rotation axis used the optic chiasm to facilitate identification of the position of the eyeball and grasp of the rotation state. The y-axis was set parallel to both eyeballs, as shown in Figure 1C. In addition, the x-axis was set orthogonal to the y-axis. The z-axis was vertically set as the working reference plane, orthogonal to the x- and y-axes. To create a shape that ensured that the crystalline lenses of both eyes appeared the same, the x-axis was rotated. Then the y-axis was rotated so that the anterior chamber is at its greatest depth. Finally, the z-axis was moved up and down so that the crystalline lens could attain its maximum size. In this study, the MRIs from the 1.2- to 3-mm slices were used.

In the evaluation and examination, the measurement of AL by A-scan ultrasonography (AL-3000; TOMEY, Nagoya, Japan) was compared in seven subjects (14 eyes) with that based on the MRI. The MRI of the 3-mm slice was used for evaluation and examination to ensure an error margin for the region. Because the AL based on the MRI did not contain the corneal thickness, AL based on A-scan ultrasonography was a value from which the corneal thickness had been subtracted. The results of the MRI validation are shown in Table 1. AL determined by A-scan ultrasonography showed a significant correlation with that generated by the unprocessed MR (Pearson $r = 0.956$; $P < 0.001$) and 3D restructured ($r = 0.966$; $P < 0.001$) images. A Bland-Altman plot, indicating the relationship between AL generated by the unprocessed MR and 3D restructured images with that based on A-scan ultrasonography was made, as shown in Figure 2. Because the horizontal image of the unprocessed MRI did not usually cut an eyeball at a major axis, AL determined from the unprocessed MRI was shorter than the actual length (Table 1). In addition, there was a significant difference between the error margin of AL determined by a combination of A-scan ultrasonography and the 3D-restructured image and the error margin of AL determined by a combination of A-scan ultrasonography and the unprocessed MRI (paired t-test, $P = 0.0191$). In this study, therefore, we used the T_2-weighted horizontal MRIs that used the 3D restructuring technique to estimate the geometry of the eyeball.

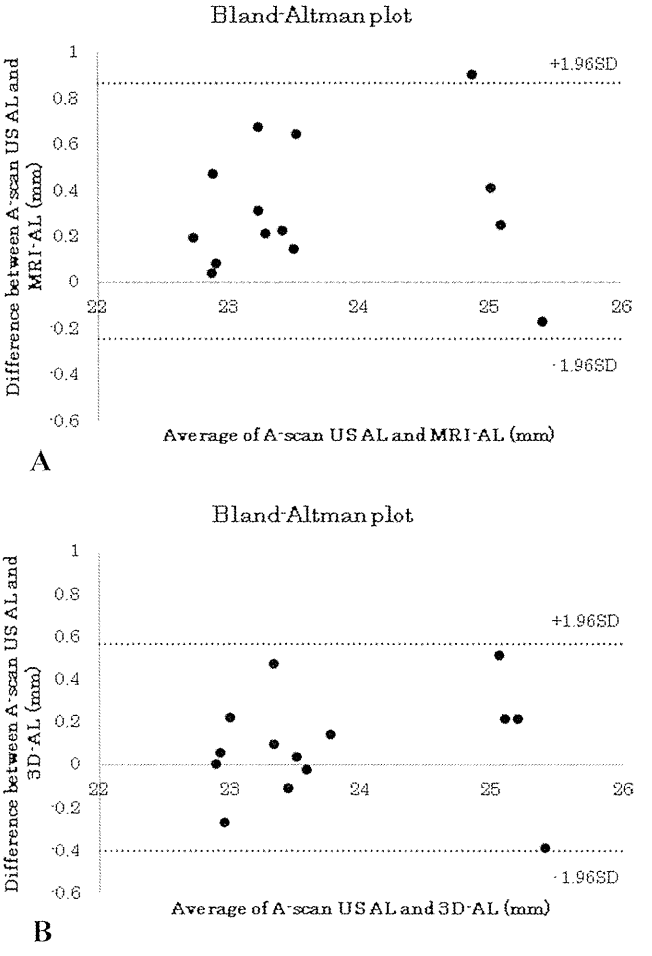

FIGURE 2. Bland-Altman plots indicating the relationship between AL generated by the unprocessed MR and 3D restructured images and that based on A-scan ultrasonography. A-scan US, A-scan ultrasonography. (**A**) The mean value of the difference between the A-scan-US AL and MRI AL was 0.31. The average difference ±1.96 SD was from −0.24 to 0.87. (**B**) The mean value of the difference between the A-scan-US AL and 3D AL was 0.081. The average difference ±1.96 SD was from −0.40 to 0.57.

Elliptic Fourier Descriptors

To obtain a sharply defined contour of the eyeball, the T_2-weighted MRIs were used for elliptic Fourier descriptors (EFDs; Fig. 3A). In all cases, images of the right eyes were used for image processing and contour recording. In the derivation of EFDs, the x- and y-coordinate information of the contour of eyeball was taken in the form of a closed curve, as is illustrated in Figure 3B. The shape was mathematically delineated with the Fourier series expansion of the closed curve. The obtained Fourier coefficients (a_n, b_n, c_n, and d_n) were further standardized to be invariant under a change of size and direction of a contour and starting point of contour trace. In this study, standardization was done on the basis of the two landmark points that were used in axial length measurements. In standardizing EFDs, the corneal apex of the right eye was placed on the right, the temporal side on the top, and the nasal side at the bottom (Fig. 3C).

With regard to the harmonic number n, the larger the maximum value of n becomes, the better the descriptive power of the shape. In this analysis, the value of n was set at 20 ($n = 20$). When $n = 20$, the standardized EFDs comprise 80 standardized Fourier coefficients. Since the number of coefficients was large, it was not easy to analyze the variation of each coefficient and understand the results of the analysis.

To summarize the information contained in the EFDs, we conducted a principal component analysis (PCA) of EFDs. The PCA reduced the dimension of the original data (i.e., 80) to a much lower dimension. The PCA was performed based on the variance-covariance matrix of the coefficients, and the component scores of the first several components were used as the measurements of the eyeball shape (Fig. 3D). The shape analysis method that uses standardized EFDs evaluates the shape provided from an eyeball image (such as Fig. 3A) by several shape principal components (s_1, s_2, s_3, ...), as shown in Figure 3D.

Evaluation of Oblateness

Oblateness indicates the shape of a spheroid body compared with that of a sphere. Oblateness f is defined as $f = 1 - \mathrm{AL}/a$, where a is the equatorial diameter. For an oblate spheroid for which $a > \mathrm{AL}$, $f > 0$, and for a prolate spheroid for which $a < \mathrm{AL}$, $f < 0$. For a sphere, $f = 0$.

Statistical Analyses

The measurements of the eye dimensions of AL and width were recorded in millimeters and are expressed as the mean ± standard deviation. The Pearson correlation coefficients, determined using a bivariate correlation analysis, were used to compare factors such as AL,

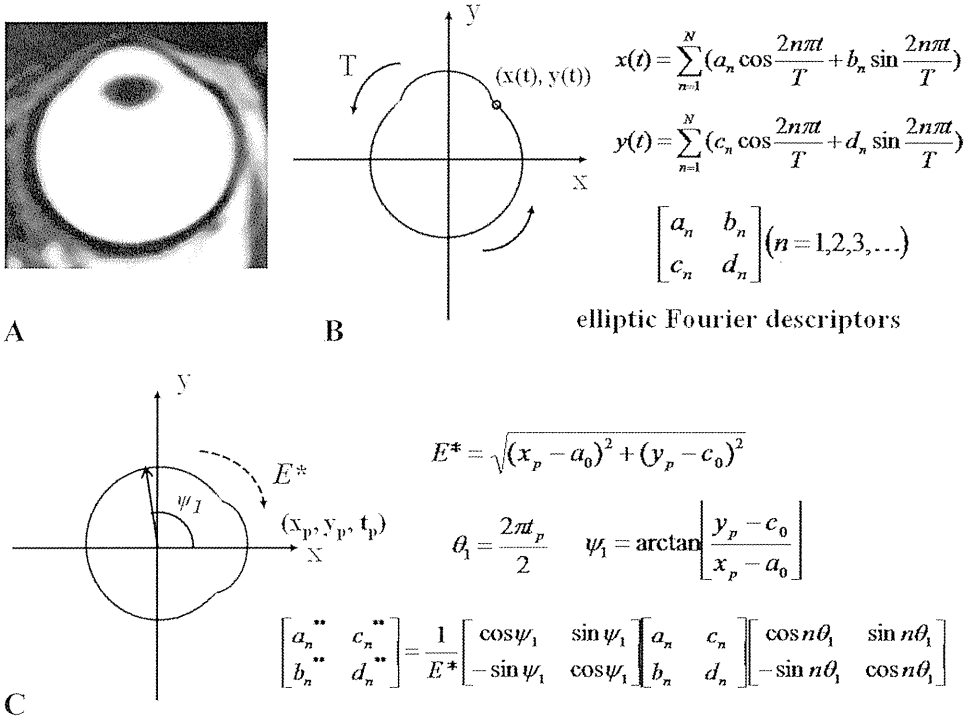

FIGURE 3. (**A**) In reference to the T_2-weighted MRIs that were obtained of the right eye. (**B**) The closed curve on the graph refers to the seam of the contour that was image processed from the eyeball images derived via MRI. The x and y coordinates of the contour are delineated, respectively, as periodic functions of distance t with a period of T. (**C**) The location of point E^* on the graph, which is a reference point for standardizing the elliptic Fourier descriptors obtained in (**B**) was identified manually. With this standardization, the size and direction of all contours were aligned, respectively, to the size and direction of the corneal apex on the right eyeball. (**D**) A PCA was performed based on the variance-covariance matrix of the coefficients.

width, age, principal components of standardized EFDs, and oblateness. $P \leq 0.05$ was significant (StatView ver. 5.0; SAS, Cary, NC).

RESULTS

There were 105 patients (105 eyes) enrolled in the study; they consisted of 55 males and 50 females, ranging in age from 1 month to 19 years (8.47 ± 6.64 years). The AL (Pearson r = 0.794; $P < 0.001$) and width (r = 0.754; $P < 0.001$) of the right eyes showed a significant correlation with age. AL and age were closely approximated via a logarithmic approximation. AL (Pearson $r = -0.443$; $P < 0.001$) and age ($r = -0.356$; P = 0.002) showed a significant correlation with oblateness (Figs. 4A, 4B). The average of the spherical equivalent refraction (SER) was −0.68 ± 1.19 D (n = 30). The SER showed a significant correlation with AL ($r = -0.695$, $P < 0.001$), width ($r = -0.547$; P = 0.0014), oblateness (r = 0.423; P = 0.0189), and age ($r = -0.682$; $P < 0.001$).

A PCA was performed based on the variance-covariance matrix of the coefficients (Fig. 3D). Therefore, each principal component was independent of the shape without the correlation. In the PCA of standardized EFDs, the proportion of the variance/total variance of the first principal component (PC1) was 76.0%. The proportions of PC2 and PC3 were 7.7% and 4.1%, respectively. Figure 5 shows the changes in shape variations within the value range of −2 to 2 SD for the three principal components. The solid line in Figure 5 indicates the average value, and the numerical value is set at 0 in the PCA. The dotted line represents −2 SD, and the dashed line represents 2 SD. Regarding the components following PC4, their ratio to the eyeball shape was small, and the change was minute. As a result, it was found that PC1 showed a significant correlation with age (Pearson $r = -0.314$; P = 0.001) as well as with AL ($r = -0.378$; $P < 0.001$), width ($r = -0.200$; P = 0.0401), and oblateness (r = 0.657; $P < 0.001$; Fig. 4C). PC1 also was significantly correlated with SER (r = 0.438, P = 0.0146; n = 30). PC2 showed a significant correlation with oblateness (Pearson $r = -0.289$, P = 0.0027), but not AL (Fig. 4D). PC1 and -2 almost intersected oblateness in the origin (Figs. 4C, 4D). Therefore, the eyeball shape of the mean value of PC1 and -2 was approximately spherical.

Emmetropization is usually completed by about age 6 years. For those subjects in the group aged 1 month to 6 years (n = 49), AL (Pearson r = 0.733; $P < 0.001$), width (r = 0.681; $P < 0.001$), and oblateness ($r = -0.309$; P = 0.0301) showed a significant correlation with age. PC1 showed a significant correlation with AL ($r = -0.421$; P = 0.0024), oblateness ($r = -0.715$; $P < 0.001$), and age ($r = -0.366$; P = 0.0093), whereas PC2 only showed a significant correlation with oblateness ($r = -0.355$; P = 0.0118). The average SER of the younger subjects was 0.09 ± 0.75 D (age, 1 month–6 years; n = 14). For those subjects aged 7 to 19 years (n = 56), AL (r = 0.459; P = 0.003) and width (r = 0.312; P = 0.0187) showed a significant correlation with age. This result seems to reflect

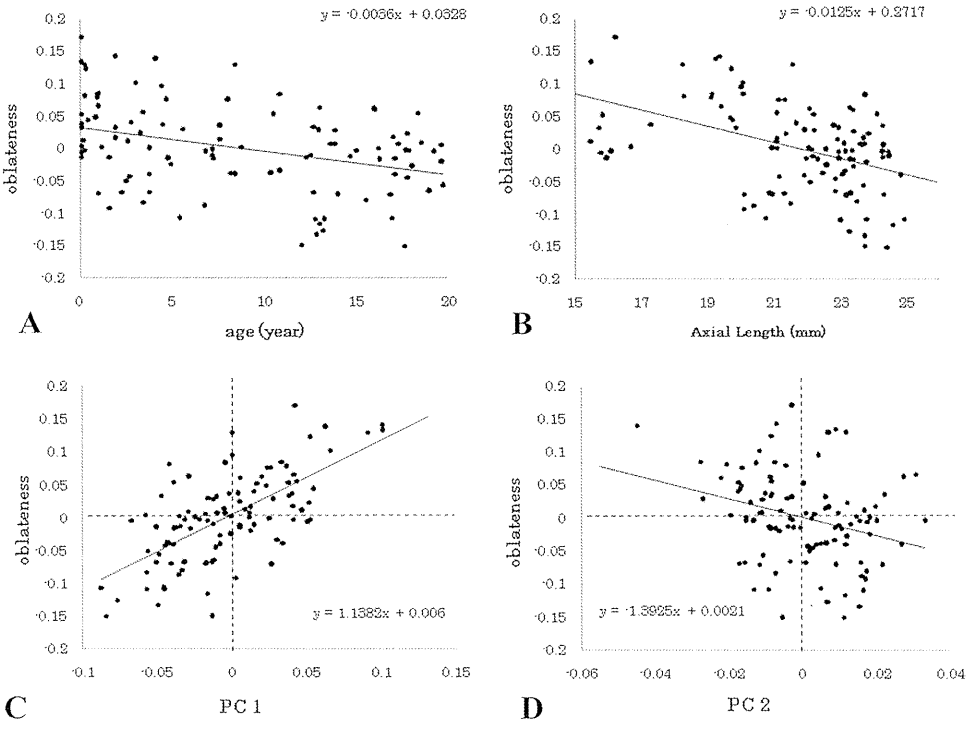

FIGURE 4. Scatterplots indicating the relationship between oblateness, age, axial length, and PC1 and -2 (**A**, **B**). Age (Pearson $r = -0.356$; $P = 0.002$) and axial length ($r = -0.443$; $P < 0.001$) showed a significant correlation with oblateness. (**C**) PC1($r = 0.657$; $P < 0.001$) and (**D**) PC2 ($r = -0.289$; $P = 0.0027$) showed a significant correlation with oblateness. PC1 and -2 almost intersected oblateness in the origin. Therefore, the eyeball shape of the mean value of PC1 and -2 was approximately a sphere.

the trend of increasing myopia with increasing age within this subject population. PC1 showed a significant correlation with oblateness ($r = -0.524$; $P < 0.001$). The average SER of the young adult subjects was -1.36 ± 1.11 D (age, 7–19 years; $n = 16$). PC1 showed a significant correlation with SER ($r = 0.640$; $P = 0.0063$), as did oblateness ($r = 0.534$, $P = 0.0317$). The correlations between PC1 and -2 in the two age groups and AL, width, oblateness, age, and SER are summarized in Table 2. Figure 6 shows the scatterplots comparing PC1 with age and SER in the two age groups.

Discussion

To quantitatively evaluate the patterns of development of the shape of the eyeball, we performed PCA using standardized EFDs from the MRIs of 105 right eyes. The significance of PC1 and -2 in such development, which can be understood by visualizing the aforementioned PCA, is shown in Figure 5. Such visualization helps us to understand the morphologic meaning of each principal component axis, which is not easy to do in a multivariate analysis.[17] In addition, visualization may give us an idea for a novel shape characteristic that has not been evaluated so far.

PC1 is the width expansion and contraction. The oblateness showed a significant correlation with AL and PC1 (Figs. 4B, 4C). In addition, PC1 showed a significant correlation with age. Therefore, the deformation pattern of PC1 in the development of the shape of the eyeball was thought to be a change from oblate to prolate (i.e., a gradual change in the eyeball to a spherical shape from an oblate one and to a prolate shape from a sphere). This result shows the extension of AL to be more dominant than the extension of the width in the development of the eyeball. While the findings associated with myopic changes were consistent with those of many previous reports,[1,5–7] few studies have addressed the eyeball transformation pattern in emmetropization, most likely because most evaluations of the eyeball shape of emmetropia have been conducted during later childhood.[1,7]

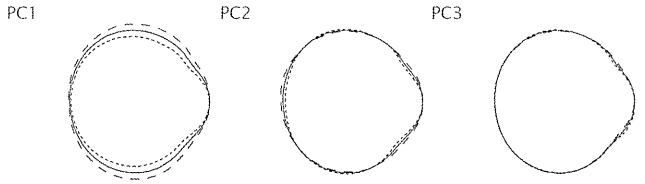

FIGURE 5. Eyeball images where the PCA by standardized EFDs was visualized. Shape variations were accounted for by the first three principal components. Contours drawn in *solid lines* are the average shape, and the numerical value is set to 0 in the PCA. Contours drawn in *dotted* and *dashed lines* correspond to shapes having the component scores of -2 and 2 SD, respectively.

PC2 is the posterior pole elongation (Fig. 5). It should be noted that the oblate-to-prolate change cannot be evaluated accurately in terms of oblateness alone. However, oblateness was correlated with both PC1 and -2 according to this examination (Fig. 4). Therefore, since oblateness is an evaluation made using the ratio, the true oblate-to-prolate change and posterior pole elongation cannot be distinguished. That the difference of the shape variation cannot be evaluated by the ratio, but can be distinguished, is one of the advantages of using EFDs in this research.

A major advantage of shape analysis based on the principal components of EFDs is that it requires no prior knowledge about morphologic variations of analysis objects. As suggested by PC2 estimated in this study, we were able to discover a novel shape characteristic and measure it via the shape analysis without any prior knowledge. On the other hand, in analyses based on conventional shape characteristics, we should identify characteristics that are appropriate for evaluating analysis objects by referring to previous studies before taking measurements (e.g., the ratio of the length and the radius of curvature).[1,5–7] If the established characteristics are not appropriate for our analysis objects, the shape variations of those objects will not be adequately evaluated. It should be noted that EFDs are not necessarily summarized by PCA alone. Other multivariate analysis methods may also be useful to extract significant information for our study objectives from EFDs. To evaluate

TABLE 2. Correlation Coefficients between PCA of Eyeball Shape and Geometric Data, Age, and Refraction in the Two Age Groups

Age Group	Principal Component	AL	Width	Oblateness	Age	SER (n = 30)
1 mo–6 y (n = 49)	PC1	−0.421*	−0.205	0.715†	−0.366*	0.015
	PC2	−0.134	−0.266	−0.355‡	−0.108	−0.251
7–19 y (n = 51)	PC1	−0.200	0.227	0.524†	−0.173	0.640*
	PC2	0.232	0.097	−0.161	−0.147	0.329

Data are expressed as Pearson's correlation coefficient.
* $P < 0.01$.
† $P < 0.001$.
‡ $P < 0.05$.

local shape characteristics, such as the shape of the corneal or retinal surfaces, more precisely, a different approach may be necessary. One example of such an evaluation method is measuring the angle of the tangent on the retinal surface and the Q-value.[4,8]

The main result of this study is that there are clear differences between age groups with regard to changes in the shape of the eyeball, the correlation between these changes, and changes in refractive status. At 6 years of age, when emmetropization is generally complete, PC1 showed a significant negative correlation with age, but not with SER (Figs. 6A, 6C). Previous studies have generally assumed that visual signals processed in the fovea dominate the emmetropization process and are the genesis of common refractive errors in children.[18] From our results, it was not possible to explain changes in the shape of the eyeball during the emmetropization period by using the refraction value alone. Therefore, the pattern of development of the shape of the eyeball during emmetropization was thought to be a fixed form change from the oblate shape to the sphere (i.e., oblateness is 0 at approximately 6 years of age; Fig. 4A). During the period from age 7 to 19 years, PC1 showed a significant correlation with SER, but not with age (Figs. 6B, 6D). To explain the fact that the oblate-to-prolate changes did not correlate with age, we proposed that the main eyeball shape transformation after age 7 is global expansion. In a past report, the shape of the eyeball in adult eyes was almost the same as that described for emmetropia.[5] In contrast, another past study indicated that myopic eyes in children are typically prolate.[1] Our results showed that the development of myopia was due to the oblate-to-prolate change that occurred during the period from 7 to 19 years of age (Fig. 6D).

Recent studies have suggested that the mouse eye grows in two phases—that is, a period of rapid growth that lasts until postnatal day (P)40 to P60 and a period of very slow eye expansion that continues up to P300.[19,20] When the evaluation of the crystalline lens and corneal radius of curvature were added, Tkatchenko et al.[21] suggested that the mouse eye grows in three phases. In the human eye, AL has a growth pattern approximated in the logarithmic function, with a rapid growth phase up to 6 years of age followed by a slow growth phase from 6 years onward.[22,23] Our research results suggest that there is a difference in the development of the shape of the eyeball between these two phases of growth. In addition, the change in the eyeball shape did not essentially correlate with age in the young adult subjects. On the other hand, the change from oblate to prolate was shown in the myopic subjects

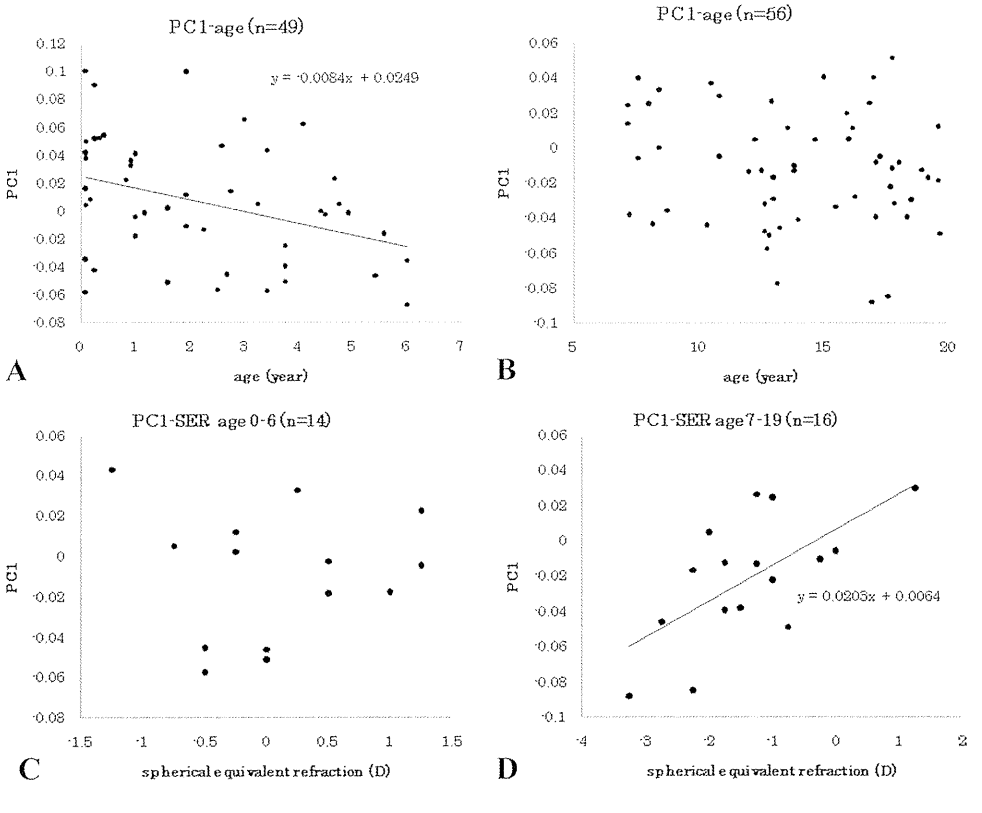

FIGURE 6. Scatterplots indicating the relationship of PC1 with age and SER in the two age groups. (**A**, **C**) In those subjects aged 1 month to 6 years, PC1 showed a significant negative correlation with age (Pearson r = −0.366; P = 0.0093), but not with SER. (**B**, **D**) In those subjects aged 7 to 19 years, PC1 showed a significant correlation with SER (r = 0.640; P = 0.0063), but not with age.

during the period from 7 to 19 years of age. Therefore, it was suggested that two pattern changes in the eyeball shape exist in the young adult subjects.

There were some limitations in this study. One constraint was the possibility that the sample data were biased because the subjects were not prospectively selected randomly. Another potential limitation is that, since only the horizontal images were examined, the overall height of the eyeball was not known. It is necessary to examine the MRI in a slice of 1 mm or smaller to restructure the sagittal image with the horizontal image.[24] Because this examination was part of a retrospective study, it was difficult to obtain other data. In addition, the cases that had an appreciable refractive error were limited. If it had been possible to examine patients by subdividing them into those with emmetropia and those with myopia, a more interesting result might have been obtained.

In conclusion, the main deformation pattern in the development of the shape of the eyeball from oblate to prolate was clarified by quantitative analysis based on EFDs. Our findings suggest that there are differences between age groups with regard to changes in the shape of the eyeball, the correlation between these changes, and changes in refractive status. Previous studies were unable to evaluate complex shapes, such as that of the entire eyeball. This research clearly distinguished two or more deformation patterns of the eyeball shape that could not be distinguished by the aspect ratio (i.e., the oblate-to-prolate change, the posterior pole elongation, and the global expansion). We believe that our new technique based on EDFs, which allows quantitative evaluation of the shape, is effective for research on emmetropization and myopic changes and will ultimately serve as a useful tool in the field of ophthalmology.

References

1. Mutti DO, Sholtz RI, Friedman NE, Zadnik K. Peripheral refraction and ocular shape in children. *Invest Ophthalmol Vis Sci.* 2000;41:1022–1030.
2. Mutti DO, Mitchell GL, Jones LA, et al. Axial growth and changes in lenticular and corneal power during emmetropization in infants. *Invest Ophthalmol Vis Sci.* 2005;46:3074–3080.
3. Mutti DO, Hayes JR, Mitchell GL, et al. Refractive error, axial length, and relative peripheral refractive error before and after the onset of myopia. *Invest Ophthalmol Vis Sci.* 2007;48:2510–2519.
4. Zhu L, Bartsch DU, Freeman WR, Sun PC, Fainman Y. Modeling human eye aberrations and their compensation for high-resolution retinal imaging. *Optom Vis Sci.* 1998;75:827–839.
5. Deller JFP, O'Connor AD, Sosby A. X-ray measurement of the diameters of the living eye. *Proc R Soc Lond B Biol Sci.* 1947;134:456–467.
6. Atchison DA, Jones CE, Schmid KL, et al. Eye shape in emmetropia and myopia. *Invest Ophthalmol Vis Sci.* 2004;45:3380–3386.
7. Song HT, Kim YJ, Lee SJ, Moon YS. Relations between age, weight, refractive error and eye shape by computerized tomography in children. *Korean J Ophthalmol.* 2007;21:163–168.
8. Atchison DA, Pritchard N, Schmid KL, Scott DH, Jones CE, Pope JM. Shape of the retinal surface in emmetropia and myopia. *Invest Ophthalmol Vis Sci.* 2005;46:2698–2707.
9. Kuhl FP, Giardina CR. Elliptic Fourier features of a closed contour. *Comp Graphics Image Processing.* 1982;18:236–258.
10. Iwata H, Niikura S, Matsuura S, Takano Y, Ukai Y. Evaluation of variation of root shape of Japanese radish (Raphanus sativus L.) based on image analysis using elliptic Fourier descriptors. *Euphytica.* 1998;102:143–149.
11. Iwata H, Niikura S, Matsuura S, Takano Y, Ukai Y. Diallele analysis of root shape of Japanese radish (Raphanus sativus L.) based on elliptic Fourier descriptors. *Breed Sci.* 2000;50:73–80.
12. Iwata H, Ukai Y. SHAPE: A computer program package for quantitative evaluation of biological shapes based on elliptic Fourier descriptors. *J Hered.* 2002;93:384–385.
13. McLellan T. The roles of heterochrony and heteroblasty in the diversification of leaf shapes in Begonia dregei (Begoniaceae). *Am J Bot.* 1993;80:796–804.
14. Ohsawa R, Tsutsumi T, Uehara H, Namai H, Ninomiya S. Quantitative evaluation of common buckwheat (Fagopyrum esculentum Moench) kernel shape by elliptic Fourier descriptor. *Euphytica.* 1998;101:175–183.
15. Diaz G, Zuccarelli A, Pelligra I, Ghiani A. Elliptic Fourier analysis of cell and nuclear shapes. *Comp Biomed Res.* 1989;22:405–414.
16. Ferson S, Rohlf FJ, Koehn RK. Measuring shape variation of two-dimensional outlines. *Syst Zool.* 1985;34:59–68.
17. Rohlf FJ, Archie JW. A comparison of Fourier methods for the description of wing shape in mosquitoes (Ritera culicidae). *Syst Zool.* 1984;33:302–317.
18. Stone RA, Flitcroft DI. Ocular shape and myopia. *Ann Acad Med Singapore.* 2004;33:7–15.
19. Schmucker C, Schaeffel F. A paraxial schematic eye model for the growing C57BL/6 mouse. *Vision Res.* 2004;44:1857–1867.
20. Zhou X, Shen M, Xie J, et al. The development of the refractive status and ocular growth in C57BL/6 mice. *Invest Ophthalmol Vis Sci.* 2008;49:5208–5214.
21. Tkatchenko TV, Shen Y, Tkatchenko AV. Analysis of postnatal eye development in the mouse with high-resolution small animal magnetic resonance imaging. *Invest Ophthalmol Vis Sci.* 2010;51:21–27.
22. Scammon RE. The measurement of body in childhood. In: Harris JA, Jackson CM, Paterson DG, Scammon RE, eds. *Measurement of Man.* Minneapolis: University of Minnesota Press; 1930:173–215.
23. Gordon RA, Donzis PB. Refractive development of the human eye. *Arch Ophthalmol.* 1985;103:785–789.
24. Singh KD, Logan NS, Gilmartin B. Three-dimensional modeling of the human eye based on magnetic resonance imaging. *Invest Ophthalmol Vis Sci.* 2006;47:2272–2279.

Repeatability and reproducibility of anterior ocular biometric measurements with 2-dimensional and 3-dimensional optical coherence tomography

Shinichi Fukuda, MD, Keisuke Kawana, MD, Yoshiaki Yasuno, PhD, Tetsuro Oshika, MD

PURPOSE: To evaluate the repeatability and reproducibility of central corneal thickness (CCT), anterior chamber depth (ACD), and anterior chamber width (ACW) measurements using 3-dimensional (3-D) corneal and anterior segment optical coherence tomography (CAS-OCT) and 2-dimensional (2-D) anterior segment OCT (AS-OCT).

SETTING: Department of Ophthalmology, Institute of Clinical Medicine, University of Tsukuba, Ibaraki, Japan.

DESIGN: Nonrandomized clinical trial.

METHODS: The CCT, ACD, and ACW were measured in normal eyes using a prototype 3-D swept-source CAS-OCT device and a 2-D time-domain AS-OCT device (Visante). The coefficient of repeatability and reproducibility and the intraclass correlation coefficient (ICC) were calculated to evaluate the repeatability and reproducibility of the measurements.

RESULTS: Eighty-five eyes (85 subjects) were evaluated. The mean CCT measurement was 557.5 μm ± 40.5 (SD) with CAS-OCT and 556.4 ± 39.4 μm with AS-OCT; the mean ACD measurement, 3.13 ± 0.40 mm and 3.16 ± 0.39 mm, respectively; and the mean ACW, 11.80 ± 0.47 mm and 11.79 ± 0.49 mm, respectively. There was no statistically significant difference in CCT or ACW measurements between the 2 devices ($P>.05$, Wilcoxon signed rank test). Although the ACD measurements were significantly different ($P<.0001$), the difference was small (0.03 mm). Significant linear correlations were found between the measurements of the 2 devices ($P<.0001$). The ICC was greater than 0.99 for CAS-OCT and greater than 0.96 for AS-OCT.

CONCLUSION: Corneal and anterior segment OCT and AS-OCT provided comparable and well-correlated anterior ocular biometric measurements, with sufficient repeatability and reproducibility.

Financial Disclosure: No author has a financial or proprietary interest in any material or method mentioned.

J Cataract Refract Surg 2010; 36:1867–1873 © 2010 ASCRS and ESCRS

Although 2-dimensional (2-D) imaging is often used for image analysis in ophthalmology, 3-dimensional (3-D) imaging technology is emerging as a way to achieve more detailed assessment and better visualization of ocular structures. Three-dimensional corneal and anterior segment optical coherence tomography (CAS-OCT) was developed on the basis of swept-source OCT technology, which is a form of Fourier-domain OCT.[1,2] Fourier-domain OCT has higher sensitivity and measurement speed than 2-D time-domain OCT.[3]

A 2-D time-domain anterior segment-OCT (AS-OCT) system (Visante, Carl Zeiss Meditec) is commercially available; the system has a light source with a 1310 nm wavelength and is reported to yield highly repeatable and reproducible anterior segment measurements.[4–6] However, because of the measurement speed, 3-D images of the ocular tissue cannot be obtained. The measurement speed of swept-source CAS-OCT is more than 10 times that of 2-D time-domain OCT; furthermore, swept-source CAS-OCT provides robust protection against sample motion and thus can yield 3-D images of ocular structures.[1,7]

Arbitrary cross-sectional images of the eye's anterior segment can be obtained with 3-D CAS-OCT;

doi:10.1016/j.jcrs.2010.05.024

thus, theoretic biometric measurements of any site can be performed in arbitrary directions.[8] The repeatability and reproducibility of anterior ocular biometric measurements obtained using 3-D OCT and 2-D AS-OCT devices have not been compared; therefore, in the current study, we evaluated such measurements.

SUBJECTS AND METHODS

This study evaluated normal eyes with no ocular abnormalities except refractive error. Only the right eye of each participant was studied. The study was performed in accordance with the tenets of the Declaration of Helsinki, and all participants provided written informed consent.

Biometry Measurements

All measurements were recorded between 11:00 AM and 3:00 PM without pupil dilation. The examination room was illuminated at 6.0 ± 1.5 lux, with the illumination measured with a light meter (LM-8000, Fuso). Two experienced ophthalmologists (S.F., K.K.) sequentially obtained measurements by 3-D CAS-OCT and by AS-OCT under the same lighting conditions.

The study used the Visante 2-D AS-OCT device and a prototype 3-D CAS-OCT device built by the Computational Optics Group, University of Tsukuba and Tomey Corp.[1] The prototype is based on swept-source OCT technology, which is a derivative of Fourier-domain OCT and has the same high sensitivity and rapid measurement speed.[2,9] Swept-source OCT uses a fast-wavelength scanning-laser source and a balanced photodetector for spectrally resolved interferometric detection, which is a fundamental mechanism of Fourier-domain OCT. Standard spectral-domain OCT uses a broadband light source and a high-speed spectrometer. The light source used in the prototype 3-D CAS-OCT device has a −3 dB wavelength scanning range, which is equivalent to the −3 dB bandwidth of spectral-domain OCT (110 nm), and a center wavelength of 1.3 μm. This wavelength is longer than that of retinal spectral-domain OCT and has higher penetration into the highly scattered tissues of the anterior eye. The prototype CAS-OCT system provides 3-D visualization of the anatomic structures of the anterior segment, such as the cornea, anterior chamber, scleral spur, angle recess, and filtering bleb.[10–12] The measurement speed is 20 000 A-lines/s. The device measures tissue with a maximum width of 16.0 mm × 16.0 mm and a maximum depth of 6.0 mm. The mean axial resolution in 4.0 mm deep tissue is 11.0 μm. The lateral resolution of acquired images is less than 30.0 μm. The acquisition time is 3.3 seconds per volume for a resolution of 256 voxels × 256 voxels × 1024 voxels; the acquisition time of 256 A-scans per 1 cross-section image is 0.0129 second. A typical 3-D scan is divided into 256 horizontal cross-sections, each of which comprises 256 A-scans. This CAS-OCT system generates 2-D images by sectioning 3-D images in arbitrary directions (Figure 1, *A*, *B*, *C*, and *E*).

The 2-D AS-OCT system also has a central wavelength of 1.3 μm. With the system's standard software, the lateral resolution of acquired images is 60 μm and the axial resolution, 18 μm. The system produces anterior segment images up to 6.0 mm in depth and 16.0 mm in width. The acquisition time of 256 A-scans per 1 cross-section image is 0.125 second. On the AS-OCT images, the corneal vertex reflection is visualized as a vertical flare extending from the strong anterior corneal apex reflection.

The subjects were instructed to look at an internal fixation target during scanning with CAS-OCT and AS-OCT. On the horizontal cross-sectional slice with the corneal vertex reflection, the anterior chamber width (ACW) was measured as the distance from angle to angle (ATA) (Figure 1, *C*). On the same cross-sectional slice, a line was drawn from the ATA with a perpendicular projection that extended forward from the median point through the cornea. Central corneal thickness (CCT) and anterior chamber depth (ACD) were measured along this perpendicular line (Figure 1, *C*).[13] With the 2-D AS-OCT system, the CCT is usually measured with the dedicated cornea mode (high resolution cornea 10.0 mm wide and 3.0 mm deep); however, this mode cannot detect the angle or measure in a manner similar to that of the CAS-OCT device. The built-in caliper tool of the AS-OCT system was thus used to measure the CCT, ACD, and ACW on the horizontal cross-sectional slice with the corneal vertex reflection in anterior segment mode (Figure 1, *D*).

Statistical Analysis

Statistical analysis was performed using StatView software (version 5.0, SAS Institute, Inc.). The CCT, ACD, and ACW measurements were evaluated using Bland-Altman plots, 95% limits of agreement (LoA) (mean difference 1.96), and the Pearson correlation coefficient (r).[14] The repeatability and reproducibility coefficients and intraclass correlation coefficients (ICCs) for the measurements were assessed. The definitions of the coefficients of repeatability and reproducibility were based on those adopted by the British Standards Institution and other groups.[5,8,15,16] In brief, the coefficient of repeatability was defined as 2 standard deviations (SDs) of the differences between the measurements obtained for the same subjects obtained in a different session by the same observer. The coefficient of reproducibility was defined as 2 SDs of the differences between the measurements obtained for the same subject obtained at the same visit by different observers. The coefficients of variation were calculated from 5 consecutive CAS-OCT and AS-OCT scans by the same observer. The results of all association tests were considered statistically significant when the P value was less than 0.05.

Submitted: January 15, 2010.
Final revision submitted: April 11, 2010.
Accepted: May 26, 2010.

From the Department of Ophthalmology (Fukuda, Kawana, Oshika), Institute of Clinical Medicine, the Computational Optics and Ophthalmology Group (Fukuda, Kawana, Yasuno, Oshika), and the Computational Optics Group (Yasuno), University of Tsukuba, Ibaraki, Japan.

Supported in part by grants-in-aid for scientific research (19390439 and 19791256), Japan Society for the Promotion of Science, Tokyo, Japan.

Corresponding author: Shinichi Fukuda, MD, Department of Ophthalmology, Institute of Clinical Medicine, University of Tsukuba, 1-1-1 Tennoudai, Tsukuba, Ibaraki 305-8575, Japan. E-mail: caesar.shihtzu@gmail.com.

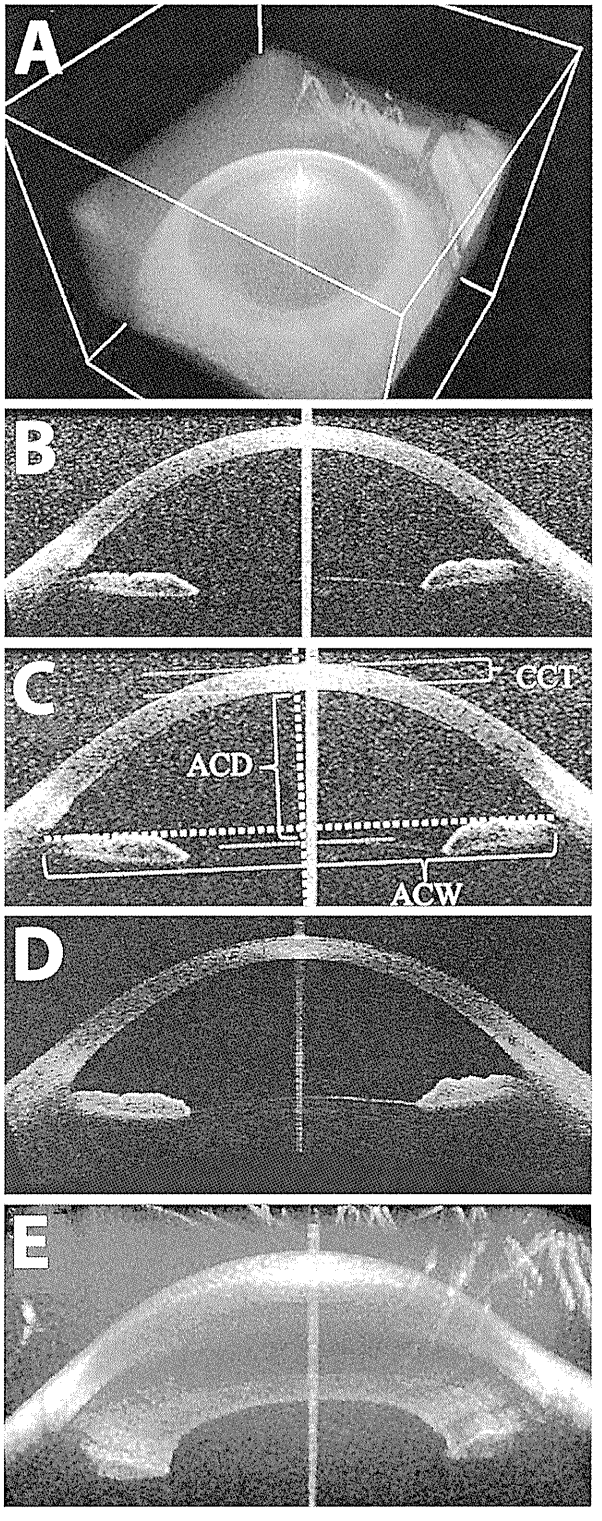

Figure 1. *A*: The 3-D image of the anterior segment obtained by CAS-OCT. *B*: Two-dimensional cross-sectional image created from the 3-D image obtained with CAS-OCT. *C*: For ACW measurement, a line is drawn from the ATA with a perpendicular projection that extended forward from the median point through the cornea. The CCT and ACD are measured along the perpendicular line. *D*: Two-dimensional cross-sectional image obtained with AS-OCT. *E*: Gonioscopic view of the anterior segment obtained with CAS-OCT (ACD = anterior chamber depth; ACW = anterior chamber width; CCT = central corneal thickness).

RESULTS

The study evaluated 85 eyes of 85 participants. The mean age of the 58 men and 27 women was 39.1 years ± 22.6 (SD) (range 22 to 89 years). The mean refractive error was −3.0 ± 2.1 diopters (D) (range −7.5 to 0.5 D).

Comparison of Measurements

Table 1 shows the mean CCT, ACD, and ACW measurements. There was no statistically significant difference in the CCT and ACW measurements between CAS-OCT and AS-OCT ($P = .128$ and $P = .608$, respectively; Wilcoxon signed rank test). Although there was a statistically significant difference in ACD measurements between the 2 devices ($P < .0001$), the difference was small (0.03 mm). There was a significant linear correlation between the CCT ($r = 0.981$, $P < .0001$), ACD ($r = 0.986$, $P < .0001$), and ACW ($r = 0.986$, $P < .0001$) measurements obtained by CAS-OCT and by AS-OCT (Figures 2 to 4).

Figures 5 to 7 show the Bland-Altman plots of the mean difference between the CCT, ACD, and ACW measurements. The 95% LoA for the CCT, ACD, and ACW measurements obtained by the 2 techniques were −12.0 to 10.1 μm, −0.07 to 0.12 mm, and −0.40 to 0.38 mm, respectively.

Repeatability and Reproducibility

Table 2 shows the repeatability and reproducibility of the CCT, ACD, and ACW measurements by CAS-OCT and AS-OCT. The repeatability and reproducibility were excellent with both devices. The ICCs for the CCT, ACD, and ACW measurements obtained using the CAS-OCT system were between 0.990 and 0.999, and these values tended to be slightly higher than those obtained using the AS-OCT system (ICC = 0.960 to 0.999).

DISCUSSION

In the current study, we compared 3-D CAS-OCT and 2-D AS-OCT systems for anterior segment biometric measurements of the eye and tested the repeatability

Table 1. Mean CCT, ACD, and ACW measurements.

	Mean ± SD		
Method	CCT (μm)	ACD (mm)	ACW (mm)
3-D CAS-OCT	557.5 ± 40.5	3.13 ± 0.40	11.80 ± 0.47
2-D AS-OCT	556.4 ± 39.4	3.16 ± 0.39	11.79 ± 0.49

ACD = anterior chamber depth; ACW = anterior chamber width; AS-OCT = anterior segment optical coherence tomography; CAS-OCT = corneal and anterior segment optical coherence tomography; CCT = central corneal thickness

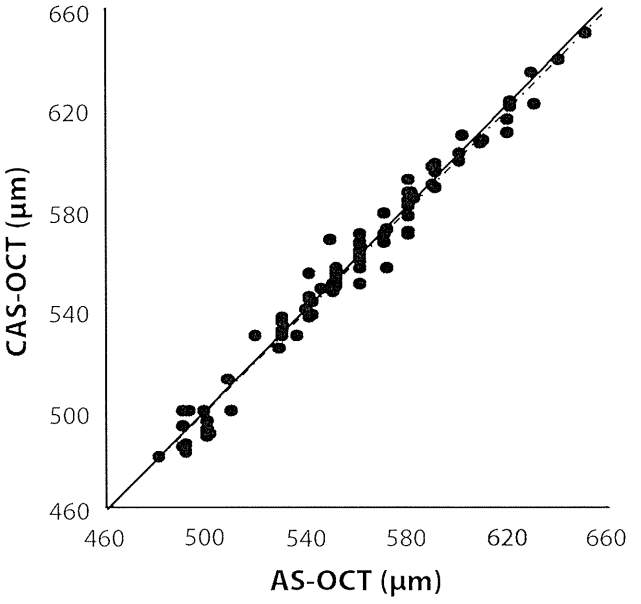

Figure 2. Correlation of CCT measurements between CAS-OCT and AS-OCT. The best-fit line ($y = -10.338 + 1.02x$) and the line of equivalence ($y = x$) are represented by the solid line and the dotted line, respectively (AS-OCT = anterior segment optical coherence tomography; CAS-OCT = corneal and anterior segment optical coherence tomography).

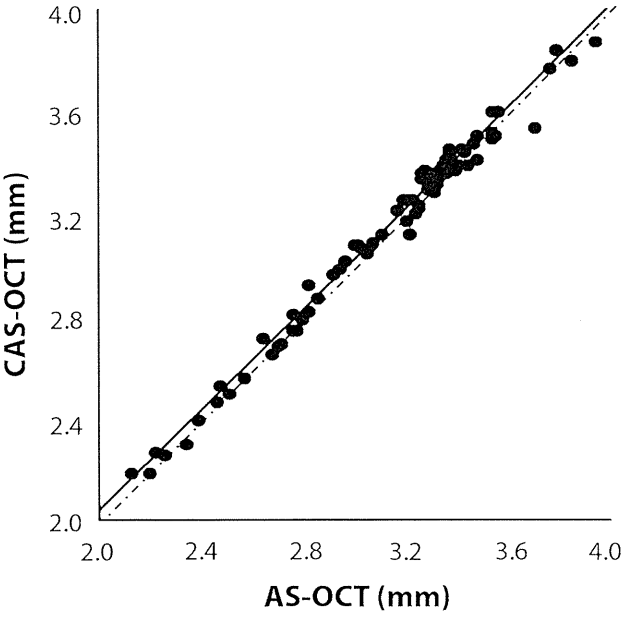

Figure 3. Correlation of ACD measurements between CAS-OCT and AS-OCT. The best-fit line ($y = 0.076 + 0.984x$) and the line of equivalence ($y = x$) are represented by the solid line and the dotted line, respectively (AS-OCT = anterior segment optical coherence tomography; CAS-OCT = corneal and anterior segment optical coherence tomography).

and reproducibility of the measurements. The CCT and ACW measurements with the 2 systems did not significantly differ; however, the ACD measurements did, although the difference was small (0.03 mm). Furthermore, the Pearson correlation test and Bland-Altman plots showed significant correlation and similarity between the 2 devices. We cannot give a definitive reason for why the only significant difference between the 2 systems was in the ACD measurements. Sometimes, the surface of the lens could not be detected on OCT images as clearly as the cornea and angle. In addition,

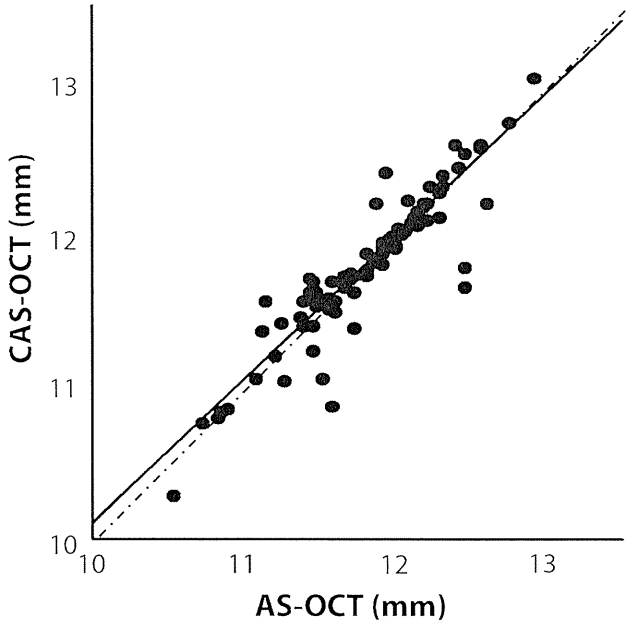

Figure 4. Correlation of ACW measurements between CAS-OCT and AS-OCT. The best-fit line ($y = 0.724 + 0.938x$) and the line of equivalence ($y = x$) are represented by the solid line and the dotted line, respectively (AS-OCT = anterior segment optical coherence tomography; CAS-OCT = corneal and anterior segment optical coherence tomography).

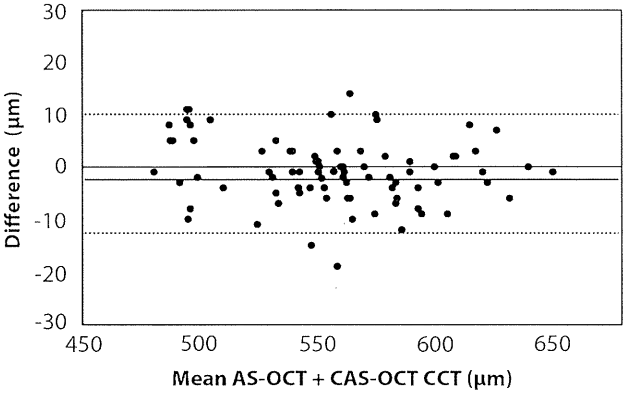

Figure 5. Bland-Altman plots of the difference from the mean in the CCT determined using CAS-OCT and AS-OCT. The mean and SD (1.96) are indicated (AS-OCT = anterior segment optical coherence tomography; CAS-OCT = corneal and anterior segment optical coherence tomography; CCT = central corneal thickness).

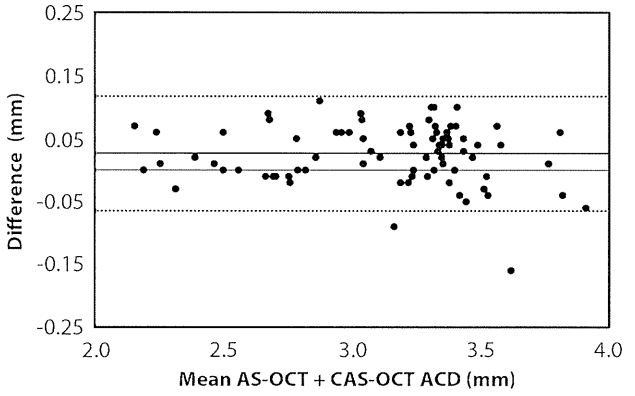

Figure 6. Bland-Altman plots of the difference from the mean in the ACD determined using CAS-OCT and AS-OCT. The mean and SD (1.96) are indicated (ACD = anterior chamber depth; AS-OCT = anterior segment optical coherence tomography; CAS-OCT = corneal and anterior segment optical coherence tomography; CCT = central corneal thickness).

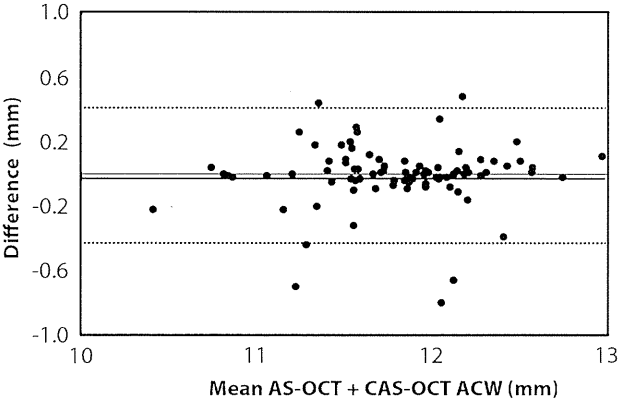

Figure 7. Bland-Altman plots of the difference from the mean in the ACW determined using CAS-OCT and AS-OCT. The mean and SD (1.96) are indicated (ACD = anterior chamber width; AS-OCT = anterior segment optical coherence tomography; CAS-OCT = corneal and anterior segment optical coherence tomography; CCT = central corneal thickness).

the difference in the depth-discrimination mechanisms of 2-D AS-OCT and 3-D CAS-OCT might account for this. Because 2D-CAS OCT is based on time-domain OCT technology, the axial motion of the sample during measurement affects the axial elongation or shortening of the OCT image more significantly. Because this effects only axial distance, it may not affect the ACW. Furthermore, the CCT is significantly smaller than the ACD; thus, the effect may not be significant. This might explain why the only AS-OCT and CAS-OCT measurements that were significantly different were those of the ACD.

Several studies of the Visante AS-OCT system[17–19] found that the CCT and ACD values obtained with the device were similar to those obtained with optical and ultrasound (US) devices. We previously reported that the CCT and ACD measurements with the CAS-OCT system had a good correlation with those of optical and US devices.[8] In a study by Li et al.,[17] the mean CCT measured using US pachymetry, scanning-slit topography, and the AS-OCT system was 553.5 ± 30.26 μm, 553.22 ± 25.47 μm, and 538.79 ± 26.22 μm, respectively. Piñero et al.[18] report mean CCT values of 528.00 ± 20.93 μm with the AS-OCT system and 527.78 ± 22.54 μm with high-frequency US scanning; both techniques had good repeatability and reproducibility. Lavanya et al.[19] compared the ACD measurements obtained with the AS-OCT device, the IOLMaster device (Carl Zeiss Meditec), and a scanning peripheral ACD analyzer; the mean values were 3.14 ± 0.34 mm, 3.08 ± 0.36 mm, and 3.10 ± 0.44 mm, respectively.

Measuring anterior chamber dimensions is important for planning ocular surgery, such as angle-supported phakic intraocular lens (pIOL) implantation.[20,21] Formerly, the size of pIOLs was determined using the white-to-white (WTW) distance. More recently, direct ACW measurements have been used to select appropriately sized angle-supported pIOLs.[18,22–24] Using an OCT system with a central wavelength of 1310 nm, Goldsmith et al.[22] found a mean ACW of 12.53 ± 0.47 mm. Kohnen et al.[23] report a mean anterior chamber diameter (equivalent to the ACW) of 12.45 ± 0.53 mm using the AS-OCT system we used in the present study; the diameter was greater than the horizontal corneal diameter, which was determined using automated WTW measurements obtained using the IOLMaster device and Orbscan IIz topographer (Bausch & Lomb). Piñero et al.[24] report a mean ATA distance of 11.76 ± 0.52 mm using the AS-OCT system; this distance significantly differed from the WTW distance measured using corneal topography. The authors concluded that these 2 parameters are not interchangeable. Thus, direct measurement of the ACW helps in the selection of an appropriately sized anterior chamber IOL.

One advantage of the 3-D CAS-OCT device in ACW measurements is that it can record 360-degree circumferences of the anterior chamber angle (ACA); thus, the ACW can be easily measured in any direction. The ACW value varies when measured in different directions. Another advantage of 3-D CAS-OCT is that it enables noninvasive gonioscopy and shows structural abnormalities in the angle of the anterior chamber[1,11]; these data are useful in planning anterior chamber IOL implantation. In addition to OCT, US biomicroscopy has been used to measure the ACW and visualize the ACA.[25] However, US biomicroscopy requires direct contact between the probe and the eye. In addition, accurate cross-sectional imaging of the anterior chamber is difficult with the technique.

Table 2. Repeatability and reproducibility of CCT, ACD, and ACW measurements.

	CCT		ACD		ACW	
Parameter	CAS-OCT	AS-OCT	CAS-OCT	AS-OCT	CAS-OCT	AS-OCT
Repeatability						
Same day and same observer, 5 consecutive scans (n = 10)						
ICC	0.999	0.998	0.999	0.999	0.994	0.960
Coefficient of variability						
Mean	0.0019	0.0020	0.0020	0.0024	0.0024	0.0021
SD	0.0012	0.0024	0.0015	0.0011	0.0018	0.0053
Different day and same observer (n = 30)						
ICC	0.997	0.968	0.993	0.996	0.990	0.985
Coefficient of variability	5.90	20.12	0.09	0.07	0.14	0.16
Reproducibility						
Same day and different observer (n = 30)						
ICC	0.998	0.987	0.998	0.997	0.993	0.988
Coefficient of variability	5.12	12.38	0.05	0.06	0.11	0.15

ACD = anterior chamber depth; ACW = anterior chamber width; AS-OCT = anterior segment optical coherence tomography; CAS-OCT = corneal and anterior segment optical coherence tomography; CCT = central corneal thickness; ICC = intraclass correlation coefficient

In our study, the ICCs for the CCT, ACD, and ACW measurements by CAS-OCT and by AS-OCT were greater than 0.99 and 0.96, respectively. Thus, the ICC for CAS-OCT was slightly higher than that for Visante AS-OCT. The coefficients of repeatability and reproducibility tended to be better with CAS-OCT than with AS-OCT. The repeatability and reproducibility of measurements depend on consistent positioning of the eye during scanning. Both devices can monitor a subject's eye during scanning for proper positioning. In addition, CAS-OCT has an autoalignment feature; the head unit moves automatically and properly aligns the head by detecting the corneal center. Moreover, the CAS-OCT system yields 2-D images by sectioning the 3-D images in arbitrary directions, enabling rapid and easy detection of the corneal center. Previous studies[4–6,22] evaluated the repeatability and reproducibility of measurements of the anterior eye segment using OCT. Mohamed et al.[5] report that the coefficient of repeatability and reproducibility of pachymetric mapping of the Visante AS-OCT system was less than 2% in healthy individuals. Li et al.[6] found that measurements obtained with the AS-OCT system and with a slitlamp OCT system had good repeatability and reproducibility. The coefficient of variation was less than 2%, and the ICC was greater than 0.94; furthermore, the values of both OCT systems were comparable with those obtained by US pachymetry. Piñero et al.[24] found good intrasession repeatability for CCT, ACD, and ATA measurements using the AS-OCT system, with ICC values greater than 0.98.

Our study has a limitation; that is, we evaluated normal eyes only. Evaluation of diseased eyes will be the subject of future studies.

In conclusion, we evaluated the biometric measurements of the anterior eye segment by 3-D CAS-OCT and 2-D AS-OCT. The 2 techniques yielded comparable CCT, ACD, and ACW measurements with sufficient repeatability and reproducibility.

REFERENCES

1. Yasuno Y, Dimitrova Madjarova V, Makita S, Akiba M, Morosawa A, Chong C, Sakai T, Chan K-P, Itoh M, Yatagai T. Three-dimensional and high-speed swept-source optical coherence tomography for in vivo investigation of human anterior eye segments. Opt Express 2005; 13:10652–10664. Available at: http://www.opticsinfobase.org/oe/abstract.cfm?uri=OE-13-26-10652. Accessed July 19, 2010
2. Yun SH, Tearney GJ, de Boer JF, Iftimia N, Bouma BE. High-speed optical frequency-domain imaging. Opt Express 2003; 11:2953–2963. Available at: http://www.opticsinfobase.org/oe/abstract.cfm?id=77825. Accessed July 19, 2010
3. Leitgeb R, Hitzenberger CK, Fercher AF. Performance of Fourier domain vs. time domain optical coherence tomography. Opt Express 2003; 11:889–894. Available at: http://www.opticsinfobase.org/abstract.cfm?id=71990&CFID=104802408&CFTOKEN=54548817. Accessed July 19, 2010
4. Nemeth G, Vajas A, Tsorbatzoglou A, Kolozsvari B, Modis L Jr, Berta A. Assessment and reproducibility of anterior chamber depth measurement with anterior segment optical coherence tomography compared with immersion ultrasonography. J Cataract Refract Surg 2007; 33:443–447
5. Mohamed S, Lee GKY, Rao SK, Wong AL, Cheng ACK, Li EYM, Chi SCC, Lam DSC. Repeatability and reproducibility of pachymetric mapping with Visante anterior segment-optical coherence tomography. Invest Ophthalmol Vis Sci 2007; 48:5499–

5504. Available at: http://www.iovs.org/cgi/reprint/48/12/5499. Accessed July 19, 2010
6. Li H, Leung CKS, Wong L, Cheung CYL, Pang CP, Weinreb RN, Lam DSC. Comparative study of central corneal thickness measurement with slit-lamp optical coherence tomography and Visante optical coherence tomography. Ophthalmology 2008; 115:796–801. Available at: http://download.journals.elsevierhealth.com/pdfs/journals/0161-6420/PIIS0161642007007750.pdf. Accessed July 19, 2010
7. Yun SH, Tearney GJ, de Boer JF, Bouma BE. Motion artifacts in optical coherence tomography with frequency-domain ranging. Opt Express 2004; 12:2977–2998. Available at: http://www.ncbi.nlm.nih.gov/pmc/articles/PMC2752339/pdf/nihms-121054.pdf. Accessed July 19, 2010
8. Fukuda S, Kawana K, Yasuno Y, Oshika T. Anterior ocular biometry using 3-dimensional optical coherence tomography. Ophthalmology 2009; 116:882–889. Available at: http://download.journals.elsevierhealth.com/pdfs/journals/0161-6420/PIIS0161642008012761.pdf. Accessed July 19, 2010
9. Kerbage C, Lim H, Sun W, Mujat M, de Boer JF. Large depth-high resolution full 3D imaging of the anterior segments of the eye using high speed optical frequency domain imaging. Opt Express 2007; 15:7117–7125. Available at: http://www.opticsinfobase.org/oe/abstract.cfm?uri=oe-15-12-7117. Accessed July 19, 2010
10. Miura M, Kawana K, Iwasaki T, Kiuchi T, Oshika T, Mori H, Yamanari M, Makita S, Yatagai T, Yasuno Y. Three-dimensional anterior segment optical coherence tomography of filtering blebs after trabeculectomy. J Glaucoma 2008; 17:193–196
11. Kawana K, Yasuno Y, Yatagai T, Oshika T. High-speed, swept-source optical coherence tomography: a 3-dimensional view of anterior chamber angle recession. Acta Ophthalmol Scand 2007; 85:684–685. Available at: http://www3.interscience.wiley.com/cgi-bin/fulltext/118515666/PDFSTART. Accessed July 19, 2010
12. Miura M, Mori H, Watanabe Y, Usui M, Kawana K, Oshika T, Yatagai T, Yasuno Y. Three-dimensional optical coherence tomography of granular corneal dystrophy. Cornea 2007; 26:373–374
13. Dada T, Sihota R, Gadia R, Aggarwal A, Mandal S, Gupta V. Comparison of anterior segment optical coherence tomography and ultrasound biomicroscopy for assessment of the anterior segment. J Cataract Refract Surg 2007; 33:837–840
14. Bland JM, Altman DG. Comparing methods of measurement: why plotting difference against standard method is misleading. Lancet 1995; 346:1085–1087. Available at: http://www-users.york.ac.uk/~mb55/meas/dfplot.pdf. Accessed July 19, 2010
15. International Organization for Standardization. Accuracy (Trueness and Precision) of Measurement Methods and Results. Part 1. General Principles and Definitions. Geneva, Switzerland, ISO, 1994 (ISO 5725-1)
16. International Organization for Standardization. Accuracy (Trueness and Precision) of Measurement Methods and Results. Part 2. Basic Methods for the Determination of Repeatability and Reproducibility of a Standard Measurement Method. Geneva, Switzerland, ISO, 1994 (ISO 5725-2)
17. Li EYM, Mohamed S, Leung CKS, Rao SK, Cheng ACK, Cheung CYL, Lam DSC. Agreement among 3 methods to measure corneal thickness: ultrasound pachymetry, Orbscan II, and Visante anterior segment optical coherence tomography. Ophthalmology 2007; 114:1842–1847. Available at: http://download.journals.elsevierhealth.com/pdfs/journals/0161-6420/PIIS0161642007001893.pdf. Accessed July 19, 2010
18. Piñero DP, Plaza AB, Alió JL. Anterior segment biometry with 2 imaging technologies: very-high-frequency ultrasound scanning versus optical coherence tomography. J Cataract Refract Surg 2008; 34:95–102
19. Lavanya R, Teo L, Friedman DS, Aung HT, Baskaran M, Gao H, Alfred T, Seah SK, Kashiwagi K, Foster PJ, Aung T. Comparison of anterior chamber depth measurements using the IOLMaster, scanning peripheral anterior chamber depth analyser, and anterior segment optical coherence tomography. Br J Ophthalmol 2007; 91:1023–1026
20. Alió JL, de la Hoz F, Ruiz-Moreno JM, Salem TF. Cataract surgery in highly myopic eyes corrected by phakic anterior chamber angle-supported lenses. J Cataract Refract Surg 2000; 26:1303–1311
21. Pérez-Santonja JJ, Alió JL, Jiménez-Alfaro I, Zato MA. Surgical correction of severe myopia with an angle-supported phakic intraocular lens. J Cataract Refract Surg 2000; 26:1288–1302
22. Goldsmith JA, Li Y, Chalita MR, Westphal V, Patil CA, Rollins AM, Izatt JA, Huang D. Anterior chamber width measurement by high-speed optical coherence tomography. Ophthalmology 2005; 112:238–244. Available at: http://download.journals.elsevierhealth.com/pdfs/journals/0161-6420/PIIS0161642004014915.pdf. Accessed July 19, 2010
23. Kohnen T, Thomala MC, Cichocki M, Strenger A. Internal anterior chamber diameter using optical coherence tomography compared with white-to-white distances using automated measurements. J Cataract Refract Surg 2006; 32:1809–1813
24. Piñero DP, Plaza Puche AB, Alió JL. Corneal diameter measurements by corneal topography and angle-to-angle measurements by optical coherence tomography: evaluation of equivalence. J Cataract Refract Surg 2008; 34:126–131
25. Pavlin CJ, Harasiewicz K, Sherar MD, Foster FS. Clinical use of ultrasound biomicroscopy. Ophthalmology 1991; 98:287–295

First author:
Shinichi Fukuda, MD

Department of Ophthalmology, University of Tsukuba, Ibaraki, Japan

Clinical Trials

Testing of Semichronically Implanted Retinal Prosthesis by Suprachoroidal-Transretinal Stimulation in Patients with Retinitis Pigmentosa

Takashi Fujikado,[1,2] *Motohiro Kamei,*[2] *Hirokazu Sakaguchi,*[2] *Hiroyuki Kanda,*[1] *Takeshi Morimoto,*[1,2] *Yasushi Ikuno,*[2] *Kentaro Nishida,*[2] *Haruhiko Kishima,*[3] *Tomoyuki Maruo,*[3] *Kunihiko Konoma,*[4] *Motoki Ozawa,*[4] *and Kohji Nishida*[2]

Purpose. To examine the safety and effectiveness of a retinal prosthesis that is implanted semichronically in two patients with advanced retinitis pigmentosa (RP).

Methods. Two eyes of two patients with advanced RP had a retinal prosthesis implanted in a sclera pocket of one eye. The visual acuity of both eyes before the implantation was bare light perception. Phosphenes were elicited by suprachoroidal-transretinal stimulation (STS). The internal devices of the STS were implanted under the skin on the temporal side of the head, and the 49 electrode-array was implanted in the scleral pocket of one eye. Biphasic electrical pulses (duration, 0.5 ms; frequency, 20 Hz) were delivered through nine active electrodes. The threshold current was determined by currents ≤1 mA. Behavioral tasks were used to determine the functioning of the prosthesis.

Results. The surgery was completed without a retinal detachment and retinal/vitreous hemorrhage. The implanted STS system remained functional for the 4-week test period. Phosphenes were elicited by currents delivered through six electrodes in Patient 1 and through four electrodes in Patient 2. The success of discriminating two bars was better than the chance level in both patients. In Patient 2, the success of a grasping task was better than the chance level, and the success rate of identifying a white bar on a touch panel increased with repeated testing.

Conclusions. Semichronic implantation of a microelectrode-STS system showed that it was safe and remained functional for at least 4 weeks in two patients with advanced RP. (www.umin.ac.jp/ctr number, R000002690.) (*Invest Ophthalmol Vis Sci.* 2011;52:4726–4733) DOI:10.1167/iovs.10-6836

From the Departments of [1]Applied Visual Science, [2]Ophthalmology, and [3]Neurosurgery, Osaka University Graduate School of Medicine, Osaka, Japan; and [4]Nidek Co., Gamagori, Aichi, Japan.

Supported by Health Sciences Research Grants (H19-sensory-001) from the Ministry of Health, Labor and Welfare, and by the Strategic Research Program for Brain Sciences from the Ministry of Education, Culture, Sports, Science and Technology, Japan.

Submitted for publication November 3, 2010; revised January 10, February 12, and March 3, 2011; accepted March 9, 2011.

Disclosure: **T. Fujikado**, None; **M. Kamei**, None; **H. Sakaguchi**, None; **H. Kanda**, None; **T. Morimoto**, None; **Y. Ikuno**, None; **K. Nishida**, None; **H. Kishima**, None; **T. Maruo**, None; **K. Konoma**, Nidek Company (F, I, E), P; **M. Ozawa**, Nidek Company (F, I, E), P; **K. Nishida**, None

Corresponding author: Takashi Fujikado, Department of Visual Science, Osaka University Graduate School of Medicine, 2-2 Yamadaoka, Suita, Osaka 565-0871, Japan; fujikado@ophthal.med.osaka-u.ac.jp.

Retinitis pigmentosa (RP) is one of the leading causes of blindness in developed countries and is characterized by a progressive degeneration of the photoreceptors.[1,2] To restore some vision to these patients, stimulating the residual functional retinal neurons by electrical currents delivered through a retinal prosthesis is being extensively studied.[3–5]

Various types of retinal or optic nerve prosthesis have been developed, and these have been tested in animals[6–14] and patients.[15–20] A typical retinal prosthesis consists of an array of electrodes that is implanted on or beneath the retina, and it is used to deliver electrical current to the retina to stimulate functioning retinal neurons to send signals to the visual cortex, where they are perceived as light sensations called phosphenes.

We have developed a new approach for stimulating the retina called suprachoroidal-transretinal stimulation (STS).[9,21] In this method, the retinal prosthesis is placed in a scleral pocket, and the reference electrode is in the vitreous cavity. Although the distance between electrode array and the retina is not close compared with other types of retinal prosthesis, the transretinal currents can stimulate the retinal neurons effectively, and the threshold current to evoke electrically potentials from the visual cortex by the STS is comparable to that by other electrodes in animals.[21]

The ability of patients to discriminate objects visually with chronically implanted retinal prosthesis has been reported by several groups. Thus, Humayun's group reported that patients can recognize simple shapes with a 16-channel epiretinal electrode system.[18] More recently, the same group developed a chronically implantable retinal prosthesis made up of 60 electrodes. With this system, patients were able to recognize simple words (Humayun MS. *IOVS* 2010;51:ARVO E-abstract 2022). Zrenner's group implanted a 1500 channel electrode array subretinally, and the patient was able to recognize simple words or Landolt's Cs.[19,20]

Although, the resolution of the image might be lower with STS prosthesis because the electrodes are some distance from the retina, the advantage of the STS prosthesis over the epi- or subretinal prosthesis is the safety of the surgical procedures because the electrodes do not touch the retina and are stably fixed in the scleral pocket. Based on the safety of this approach, the STS system has been adopted by several other groups.[22,23] In an acute clinical trial with STS prosthesis, localized phosphenes were perceived with safety currents (≤1 mA) in two patients with advanced RP.[24]

We have developed a microelectrode-STS system that can be chronically implanted, and the purpose of this study was to determine its safety and stability when it is implanted semichronically in patients with advanced RP.

Investigative Ophthalmology & Visual Science, June 2011, Vol. 52, No. 7

TABLE 1. Patients for the Retinal Prosthesis

Patient	Age (y)	Sex	Diagnosis	Visual Acuity (Right/Left)	Years with Lowest Visual Acuity
1	72	F	RP	LP/LP	1 y
2	67	F	RP	LP/LP	17 y

F, female; RP, retinitis pigmentosa; LP, light perception.

PATIENTS AND METHODS

Retinitis Pigmentosa Patients

Two patients with RP were studied (Table 1). The diagnosis of RP was made by independent ophthalmological and eletroretinography (ERG) examinations. Patient 1 (Pt 1) was a 73-year-old woman who has had night blindness since the age of 55 years when she was diagnosed with RP. Her visual acuity decreased to hand motion in both eyes at the age of 68 years, and she had bare light perception (LP) in both eyes at 72 years at the time of these experiments. Transcorneal electrical stimulation (TES)[25] elicited phosphenes that were perceived in the central visual field with a threshold current of 0.80 mA (pulse duration, 10 ms) in the right eye and 0.65 mA (pulse duration, 10 ms) in the left eye. The area of the phosphenes increased with an increase of the stimulating current in the left eye.

Patient 2 (Pt 2) was a 67-year-old woman who has had night blindness since the age of 10 years and was diagnosed with RP at 26 years. Her visual acuity decreased to hand motion in both eyes at age 50 years and was bare LP in both eyes at the time of the surgery. TES elicited phosphenes that were perceived in the central visual field with a threshold current of 1.0 mA in the left eye and was not evoked in the right eye even with a current of 2.0 mA. The area of the phosphene did not increase with an increase in the stimulating current in the left eye.

A full explanation of the purpose of this study and the procedures to be used were given to each patient, and each signed an informed consent form. They were also instructed that they were free to withdraw at any time. The procedures used in this study adhered to the Declaration of Helsinki and were approved by the Ethics Committee of Osaka University Hospital.

Implant

The implanted electronic devices consisted of a secondary coil that receives signals from the external coil and a decoder that generates biphasic pulses to deliver to the individual electrodes sequentially (Figs. 1A, 1B). The electrode array (size, 5.7 × 4.6 mm; Nidek, Gamabori, Japan[b]) consisted of 49 electrodes made of 0.5-mm-diameter platinum wire, and the center-to-center separation of a pair of electrode was 0.7 mm (Fig. 2C). Each electrode protruded from the silicon base by 0.5 mm (Fig. 2D). The return electrode was a 0.5-mm-diameter, 6-mm-long platinum wire that was insulated except for 3 mm of the tip (Fig. 2E, 2F).

Surgical Procedures

The subjective vision was not different between the right and left eyes in both patients.

The left eye was selected for the implantation in both patients because the threshold current to elicit phosphenes by TES was lower in the left eye than in the right eye.

Under local anesthesia, the lateral rectus muscle was dissected at its insertion, and transscleral monopolar stimuli were given to determine the scleral area that consistently evoked low-threshold phosphenes.[24] After identifying and marking the low-threshold area, the patient was placed under general anesthesia. The area identified from the monopolar stimulation was relatively large and was posterior to the insertion of the inferior oblique (IO) muscle in Pt 1 and was very restricted to approximately 2 mm posterior to the insertion of the IO muscle at around 3 o'clock in Pt 2.

The skin over the left temporal bone was incised to insert the electronic devices (Fig. 1A). A second skin incision was made over the left zygomatic bone to fix the cable (see also Besch[26]; Fig. 1B). The electrode array and the return electrode were protected with a silicone cover (Fig. 2A, 2B) and passed under the fascia of the temporal muscle from the first incision to the second incision through a trocar catheter (Medikit, Tokyo, Japan).

The bone of the lateral orbital wall was drilled, and the electrode array, return electrode, and cable were passed into the periocular space using the trocar catheter. The cable with its protective cover was fixed by a titanium plate below the second incision. The electrode array and cable were circled around the equator passing under the four recti muscles.

A scleral pocket of 6 × 5 mm was made at the temporal to lower-temporal scleral area where the phosphenes were elicited. A 49-electrode array was placed in the scleral pocket (Fig. 3) and secured with sutures that passed through the protective silicone cover around the junction of the electrode array and the cable (Fig. 2D). The return electrode was inserted into the vitreous cavity through the upper nasal pars plana area.

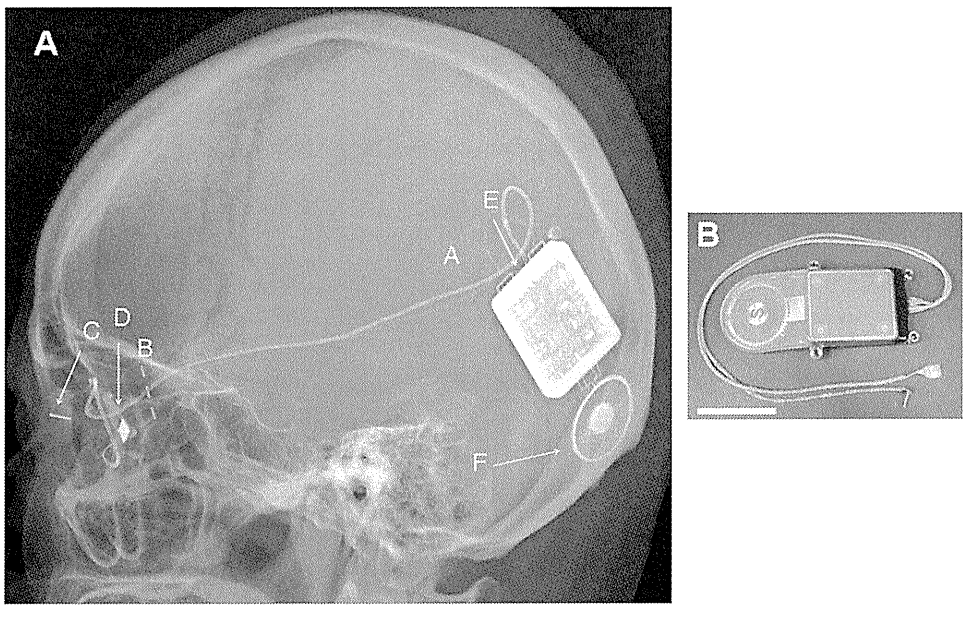

FIGURE 1. Diagram of retinal prosthesis system. (**A**) Lateral view of the skull XP of Pt 1 after implantation surgery. (A) Position of skin incision to insert and anchor the device. (B) Position of skin incision to fix the cable to the bone of the lateral orbital wall. (C) Return electrode. (D) Stimulating electrode. (E) Decoder. (F) Secondary coil. (**B**) The implanted devices, cable, and electrodes. Scale bar, 3 cm.

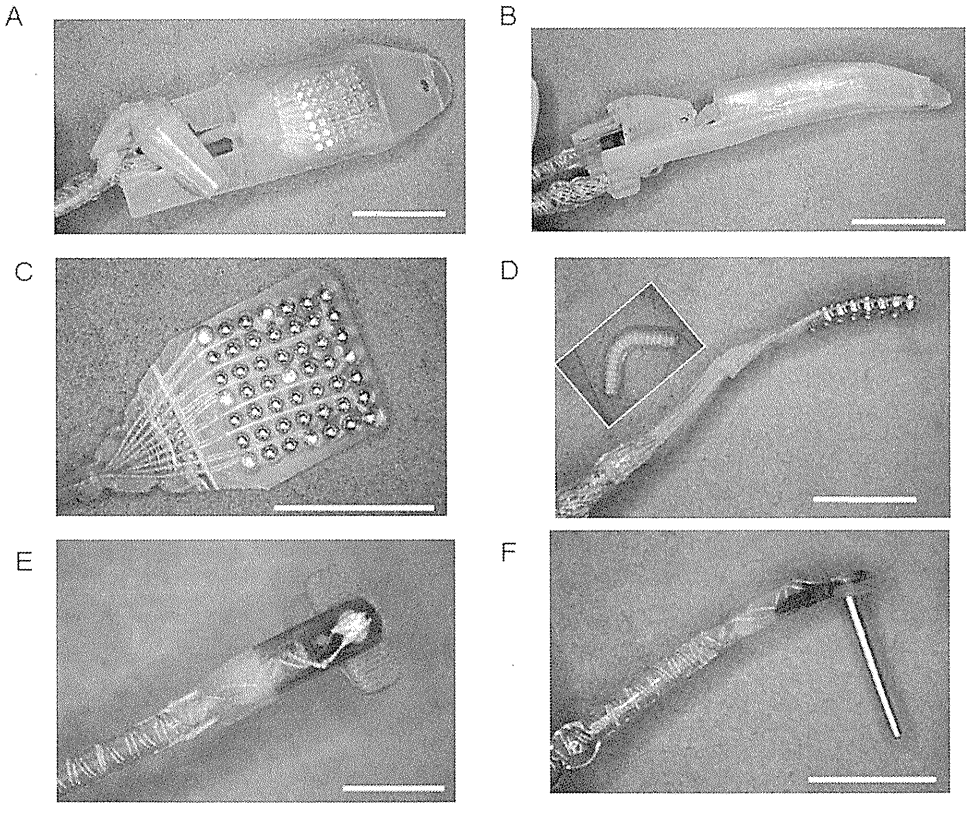

FIGURE 2. Photograph of 49-channel stimulating electrode (**A**–**D**) and return electrode (**A**, **B**, **E**, **F**). Top (**A**) and side (**B**) views of stimulating and return electrode protected by protective silicone cover. Top (**C**) and side (**D**) views of 49-channel stimulating electrode. The diameter of each electrode is 0.5 mm, and the center-to-center electrode distance is 0.7 mm. The *inset* in (**D**) shows the protective cover that reinforced the junction between the electrode array and the cable. Top (**E**) and side (**F**) views of return electrode. The diameter of return electrode is 0.5 mm. Scale bars in (**A**–**F**), 5 mm.

After suturing the conjuntival incision, the electronic device was fixed to the temporal bone, and the skin was sutured. At the end of the implant procedure, the system was tested to be certain that all electrodes were functioning. Five (Pt 1) to 7 (Pt 2) weeks after the implantation, the device and wire were surgically removed.

Functional Testing of Each Electrode

From week one after the surgery, the wireless system was tested twice a week for 4 weeks. For the functional test of each electrode, 9 out of the 49 electrodes were tested as shown in Figure 4B. The distance

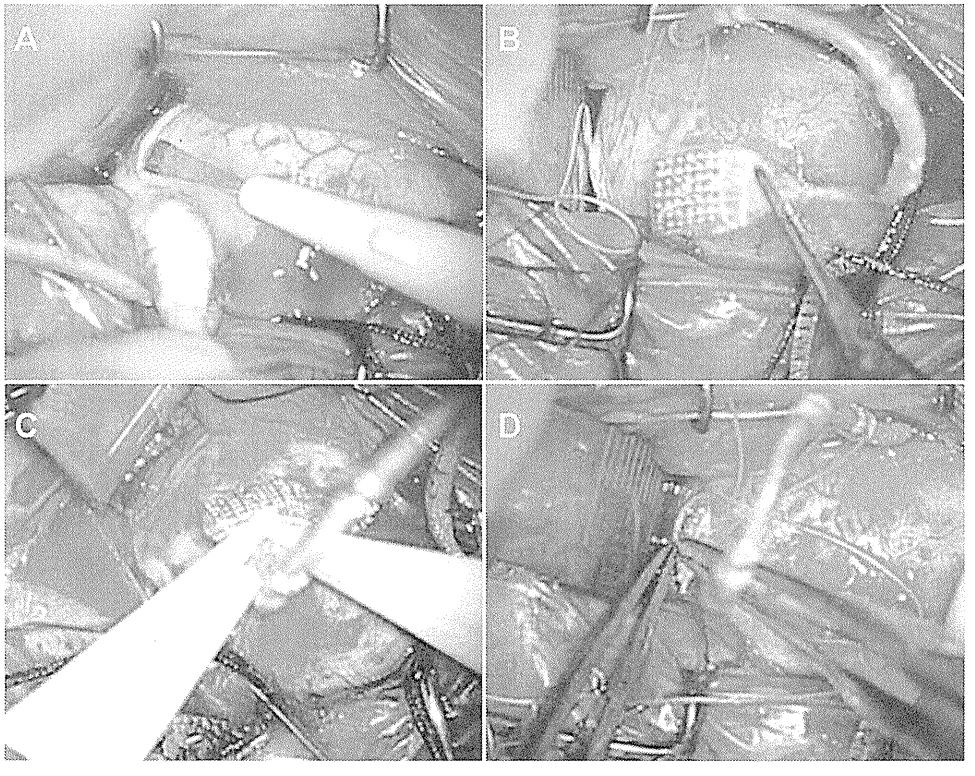

FIGURE 3. Photographs of surgical procedure to insert the electrode-array. (**A**) Creating a scleral pocket. (**B**) Holding the electrode array. (**C**) Grasping the electrode array for insertion. (**D**) Inserting the electrode array into the scleral pocket.

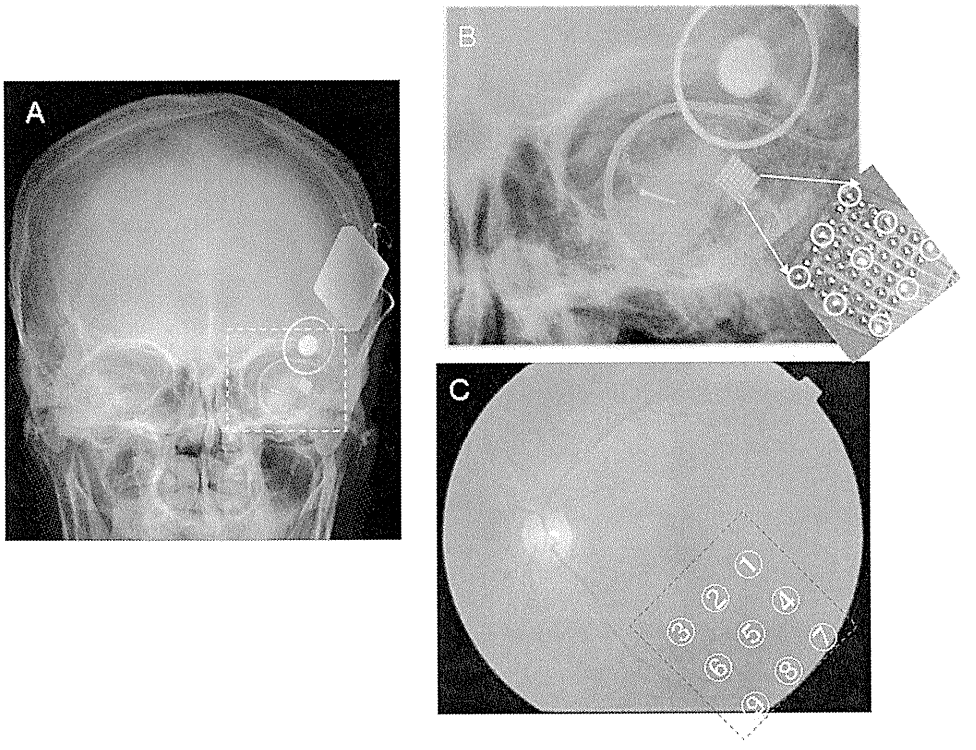

FIGURE 4. Position of the stimulating electrode. (**A**) Anterior-posterior view of the skull XP of Pt 1 after the surgery. (**B**) A magnified view of (**A**). The *insets* show the position of the nine active electrodes. (**C**) The presumed position of the none active electrodes superimposed on the left fundus of Pt 1.

between adjacent active electrode was 2.1 mm. An electronic stimulator was designed to deliver charge-balanced biphasic pulses to individual electrodes sequentially with a delay of 0.45 msec (Fig. 5). Cathodic-first biphasic pulses (duration, 0.5 ms; frequency, 20 Hz; interpulse delay, 0.5 msec; number of pulses, 20) were delivered through the selected channel or combination of multiple channels. The stimulating parameters were chosen based on the acute clinical experiment, which also used STS.[24]

The current was applied for 0.5 second after a conditioning buzzer signal. The threshold current that elicited a phosphene was determined by increasing the current intensity from 0.1 mA in 0.1 mA steps until the patients were able to recognize and localize the phosphenes correctly in >50% of the trials.

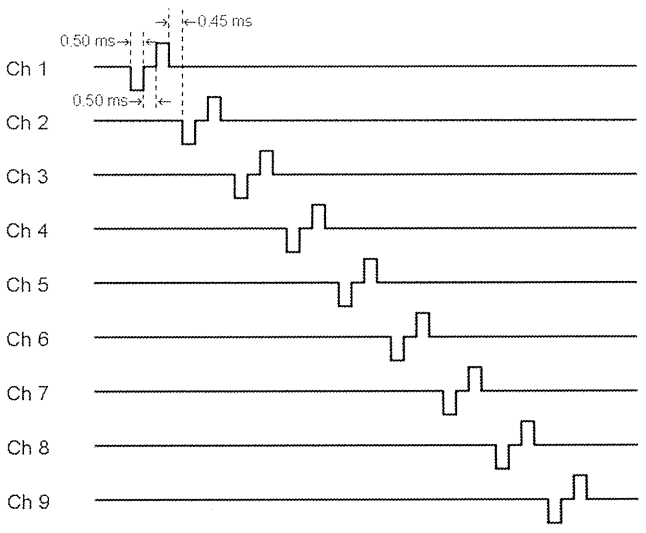

FIGURE 5. Time sequence of stimulating current pulses. The first pulse was a cathodic current, and the second pulse was an anodic current to balance the charge. A pair of pulses was delivered sequentially from channel 1 to channel 9 electrodes.

To identify the position of the phosphene, a plastic board (65 × 65 cm) was set in front of a patient at a distance of 40 cm. The patient was instructed to put her right index finger on the position of the perceived phosphene while the left index finger was positioned on the pad glued to the center of the board (Fig. 6B). For safety, the maximum current was 1.0 mA.[21] The procedure was repeated with changes in the current to determine the threshold current. Care was taken not to influence the response of the patients. The experiments to map the perceived phophenes were repeated on different days. We also tested the effect of simultaneous activation of two electrodes.

Functional Testing with Video Camera

For these experiments, the patients performed visual tasks using a commercial video camera as the detector of a visual object (QVR-13; Logitech, Tokyo, Japan). The camera was attached to a headband, and an eye mask was placed over the both eyes during the testing. Because the camera's field of view was approximately 16.7° of visual angle and the implant covered 14.3°, the visual angle subtended by an object on the retina was reduced by a factor 1.2.[18]

The object viewed by the camera was converted to a 3 × 3 square with 40 × 40 pixels, and if the light level was above the threshold, the square was expressed as white (on), and if the light level was below the threshold, the square was expressed as black (off). The information of the square was converted to an electronic signal and sent to the secondary coil through the external coil. The activated electrodes were channels (Chs) 2 to 8 (seven electrodes) in Pt 1, and Chs 1, 2, 3, 4, and 7 (five electrodes) in Pt 2.

All tests were carried out with the patients sitting on a chair and a plastic board covered with black cloths set 40 cm from the patients. The white target was presented against a black background under regular room lightning. Head movements were allowed during all experiments except in Experiment 3.

To eliminate the possibility that the patients reacted to clues other than the visual stimuli, e.g., acoustic stimuli, we performed the experiment with the electrical stimulator off but the buzzer on in each experiment. The sequence of presentation was randomized.

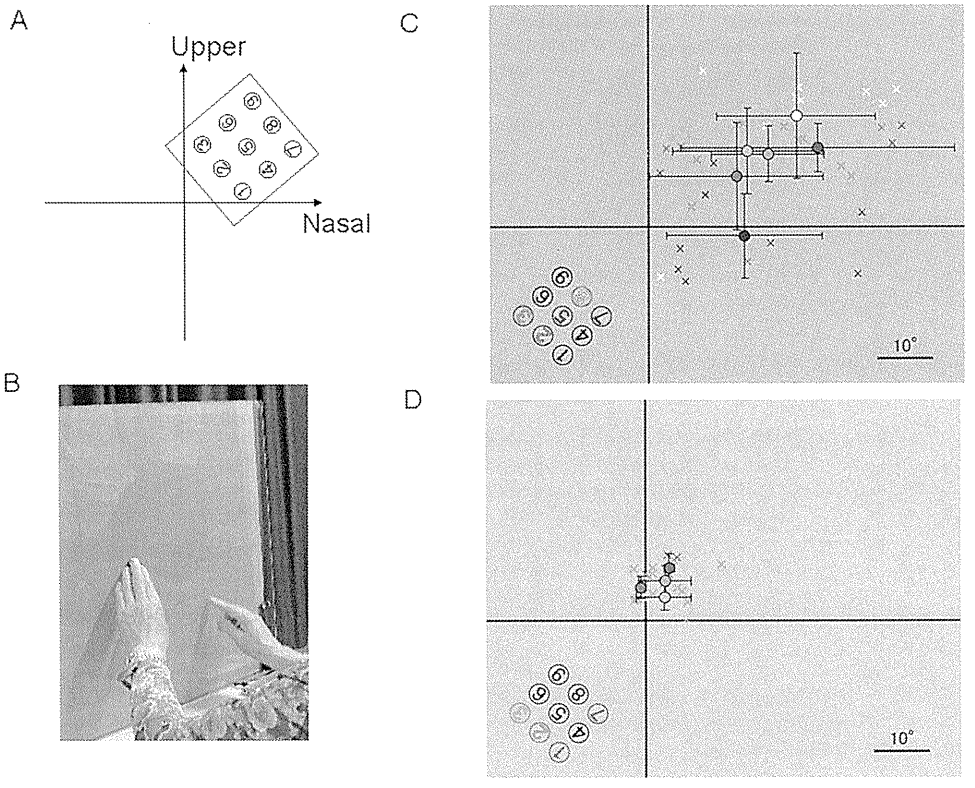

FIGURE 6. (A) Map of the perceived phosphenes in response to the stimulation of individual electrodes. The estimated position of the phosphenes when each electrode is stimulated and normal topographical organization exists between the retina and visual cortex. (B) Method to record the position of the phosphene in relation to the center of the body. The left index finger is positioned at the center of the board, and the right index finger is placed at the position of the perceived phosphene. (C) The phosphene maps of Pt 1. The results of multiple trials are superimposed. The *red, orange, green, dark blue, green, purple,* and *white* X's indicate the position of the perceived phosphene in response to the stimulation of Chs 2, 3, 5, 6, 7, and 8 individually. The *colored circles* indicate the gravitational center of the responses to the stimulation of the individual channels. The *bars* indicate the standard deviations. (D) The phosphene map of Pt 2. The *brown, red, orange, green,* and *purple* X's indicate the position of perceived phosphene in response to the stimulation of Chs 1, 2, 3, and 7.

Experiment 1: Object Detection

A white box (chopsticks box) that was 2.6 cm × 27 cm (3.7° × 34° visual angle) was set randomly at 15 cm (21°) to the left or right of the center of the board. The patients were asked where the white box was located.

Experiment 2: Object Discrimination

Two white bars of different widths, 1 cm × 30 cm (1.4°× 37°) and 3 cm × 30 cm (4.3° × 37°), were presented at the center of the board, and patients were asked to tell the examiner whether the thicker bar was on the left or right.

Experiment 3: Detection of Direction of Motion

Patients were asked to keep their head stationary. The rectangular white box (chopsticks box) was placed in front of the patients and was moved horizontally or vertically with speed 2 to 3 cm/s. The patients were asked to tell whether the bar moved horizontally or vertically.

Experiment 4: Grasping Objects

A white object was set randomly either 15 cm (21°) to the left or 15 cm to the right of the center of the board. The patient was asked to grasp the object with her right hand.

Experiment 5: Touch Panel

A white rectangular bar of 4.7 cm × 20 cm (6.7 × 27°) was presented randomly either 9.5 cm (13°) to the left or right from the center of a touch panel screen (Tyco Electronics, Menlo Park, CA) that was connected to the computer. The patient was asked to touch the white bar with her right index finger. The position touched was recorded and analyzed by the computer. Depending on whether the patient touched the correct position, a different sound was emitted by the computer.

Statistical Analyses

The percentage of correct answers on each task was analyzed statistically by the binominal test, and the criterion for statistical significance was 0.05. We tested whether each patient's performance was better than the chance level (50%) on each task. These analyses were performed with commercially available software (JMP 8.0; SAS Institute, Cary, NC).

RESULTS

Surgical Results

After surgery, it was confirmed that the device, cables, and electrodes were implanted and connected as judged by the skull x-ray projections (XPs; Fig. 1). An anterior-posterior view of the XPs of the skull showed that the electrode array was positioned at the lower temporal ocular area, and the return electrode was positioned at the upper nasal area in both patients. This was consistent with the intraoperative placements (Fig. 4).

From the fundus picture, fluorescein angiograms, and OCT images, neither retinal detachment nor hemorrhage was observed after both surgical procedures in both patients. The visual acuity remained at light perception after the removal of the device in both patients. Eye movements were slightly restricted in all directions after the initial surgery in both

TABLE 2. Threshold Stimulus Current to Evoke Electrical Phosphene

Electrode	Patient 1 (mA)	Patient 2 (mA)
Ch1	—	0.90
Ch2	0.35	0.80
Ch3	0.50	0.90
Ch4	—	—
Ch5	0.70	—
Ch6	0.60	—
Ch7	0.60	0.70
Ch8	0.60	—
Ch9	—	—

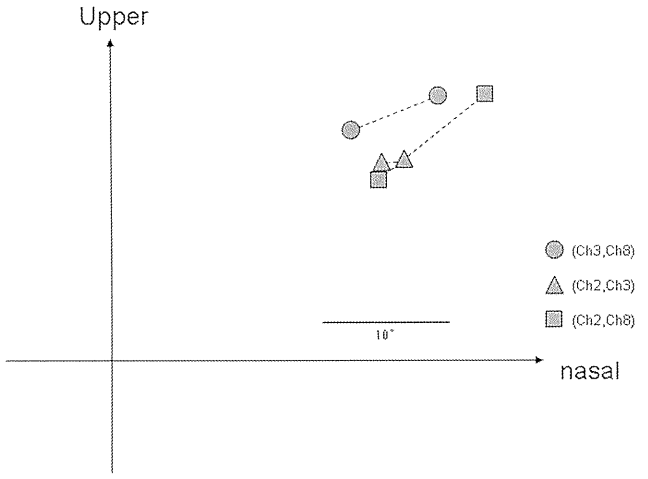

FIGURE 7. The position of the perceived phosphenes in response to simultaneous activation of two electrodes in Pt 1 (single trial). *Circles* show the position of phophenes in response to simultaneous stimulation of Chs 3 and 8, triangles to Ch 2 and 3, and squares to Chs 2 and 8.

patients but recovered in 4 weeks. The eye movements remained normal after the second surgery. The connection between the device and electrodes remained functional during the 4 weeks of testing.

Functional Testing of Each Electrode

Delivering electrical pulses from any one of the nine-electrode array elicited localized phosphenes, which were reproducible for each of the six channels (Chs 2, 3, 5, 6, 7, and 8) in Pt 1 and in four channels (Chs 1, 2, 3, and 7) in Pt 2 with current ≤1 mA (Table 2). The size of the phosphene varied from the size of a pea to a quarter coin at an arm's length distance depending on the channel stimulated in both patients. Two distinct phosphenes were perceived when the stimuli were delivered through two channels (No. 2-3, 2-8, 3-8) in Pt 1 (Fig. 6) but not in Pt 2.

The phosphenes were perceived mostly in the upper nasal field, which is consistent with the position of the stimulating electrodes in the inferior temporal quadrant (Fig. 6). The gravitational center and the standard deviation (SD) of the perceived phosphene was plotted for both patients (Fig. 5). The median value of the SD in the horizontal and vertical directions was 13.9° and 7.7 ° in Pt 1 and 2.9° and 2.5° in Pt 2, respectively. The topographical correspondence between the gravitational center of the perceived phophene and each electrode was not always consistent in both patients. The relative position of the phosphenes evoked by simultaneously activating two electrodes was almost consistent with the position and distance of electrodes in Pt 1 (Fig. 7).

Functional Testing Using a Video Camera

Both patients scored better than chance in the object detection and object discrimination tasks with head scanning. Pt 2 scored 90% better than chance in detecting the direction of motion task, but Pt 1 scored 60%, which was not significantly better than chance.

The task of grasping objects was carried out by Pt 2 because the elicited phosphene was located close to the subjective center. The score (90%) was significantly better than chance (Fig. 8).

The success rate of behavioral tasks with the electrical stimulator off was less than the chance level in each task for both patients.

The touch panel task was also applied to only Pt 2. The subjective phosphene was perceived shifted slightly to the right of the bar when presented on the right side and shifted to the left of the bar when presented on the left side. The success rate increased with repeated testing (Fig. 9).

Discussion

We implanted a retinal prosthesis in a sclera pocket of two patients with advanced RP using surgical procedures developed in experiments on dogs (Morimoto T. *IOVS* 2010;51: ARVO E-abstract 3023) and cadaver eyes. Neither a retinal detachment nor retinal bleeding was observed in both patients after the surgical procedures, confirming the safety of our surgical methods.

The connection between the internal device and the electrodes remained functioning during the 4-week testing period, indicating that the system is able to withstand the surgical manipulations and the continuous eye movements. The silicone cover of the electrode array and the return electrode helped protect the tip of the electrodes (Fig. 2A, 2B). The silicone cover at the junction between the electrode array and the cable may have also protected the wire from being disconnected during eye movements (Fig. 2D).

Eye movements were slightly restricted in all direction just after the surgery in both patients, suggesting the circumferential fixation of the cable may have affected the eye movements, which is similar to that after scleral buckling procedures. The

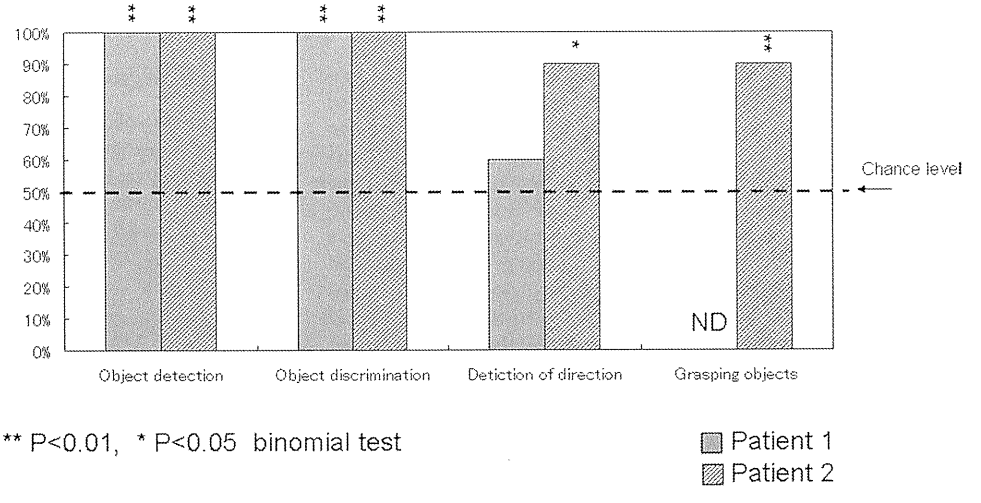

FIGURE 8. Success rate of behavioral tasks. The detection of objects was tested by 20 trials in Pt 1 and by 30 trials in Pt 2. The discrimination of object task and detection of direction were tested by 10 trials in both patients. Grasping task in Pt 2 was tested by 20 trials.

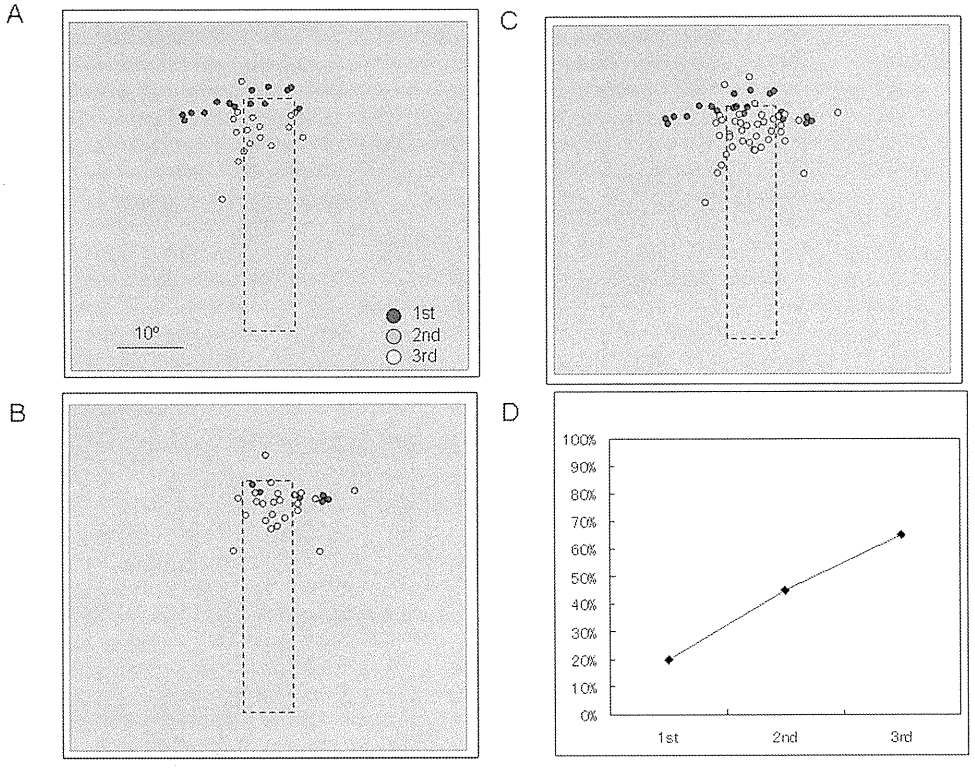

FIGURE 9. Results of the touching the panel task in Pt 2. (**A**) The touched positions when the white bar was presented on the left side. (**B**) The touched positions when the white bar was presented on the right side. (**C**) The superimposed results of (**A**) and (**B**). (**D**) The success rate after repetition of examination. The *dashed rectangular area* in (**A**–**C**) represents the position of the white bar. *Blue dots*: first trial; *pink dots*: second trial; *green dots*: third trial.

restriction was reduced 2 weeks after surgery in both patients. A transient restriction of eye movements was also reported after an implantation of a subretinal prosthesis.[26]

The position of electrode array of the STS system could not be identified directly because the electrodes were inserted in the scleral pocket and could not be observed by ophthalmoscopic examinations. However, the XP image identified the position of electrode array relative to the globe because the connecting cable was circled around the equator of the globe (Fig. 4). Gekeler et al.[27] used computed tomography for identifying the subretinal implants.

The number of electrodes that evoked phosphenes was greater in Pt 1 than in Pt 2, suggesting that more retinal neurons were preserved in Pt 1 than in Pt 2. This suggestion was supported by the fact that the threshold current determined by TES was lower in Pt 1 than in Pt 2, and the duration of the vision loss was longer in Pt 2 than in Pt 1 (Table 2). The better preservation of retinal neurons in Pt 1 is also supported by the observation that the area that could elicit a phosphene was much larger in Pt 1 than in Pt 2 during monopolar extraocular stimulation during surgery.

The position of the perceived phophenes was at the upper-nasal visual field, which is consistent with the implantation of the electrode array in the lower-temporal quadrant of the eye (Fig. 6). In Pt 2 the phophenes elicited by stimulating electrodes were located around the subjective center of the patient, suggesting that the active electrode was situated at the scleral area close to the fovea. The position of phophene was scattered in Pt 1 but relatively concentrated in Pt2. The reason for this might be that the electrodes were positioned a slight distance from the fovea in Pt 1 and close to the fovea in Pt 2. This may also account for the better repeatability in Pt 2 than Pt 1.

The position of phosphenes evoked by activating two-electrodes was consistent with the position of electrodes in Pt 1 (Fig. 7), suggesting that the localized excitation of retinal neurons was achieved by STS in this patient.

Functional testing using the CCD camera revealed that the detection and discrimination of objects were possible by head scanning with a small number of active electrodes (Fig. 8), which is consistent with the findings of epiretinal stimulation.[18] The reaching and grasping task was possible only in Pt 2, in whom the electrodes were situated close to the fovea. In the first trial, the touched position tended to shift to an area ipsilateral to the position of target. Because the patient moved her head to identify the target position and a delay of 0.1 second existed between imaging the scenery by the CCD camera and stimulating the electrode, the patient might have shifted the position of the perceived phosphene lateral to the target (Fig. 9). The success rate of the touching the panel increased after repeated testing, suggesting that a training effect may have occurred during the testing (Fig. 9D).

In summary, semichronic implantation of the electrode array–STS system showed that our approach for a retinal prosthesis is safe and feasible for artificial vision. Further improvements are necessary to achieve reading ability, and this may require increasing the number of functional electrodes.

Acknowledgments

The authors thank Yasuo Tano, Masahito Ohji, Hajime Sawai, Mineo Kondo, Tomomitsu Miyoshi, and Jun Ohta for advice and discussion and Koji Oosawa, Kenzo Shodo, Motohiro Sugiura, Akira Yabuzaki, Eiji Yonezawa, Yasuo Terasawa, Masayuki Shinomiya, Masamichi Fukasawa, Tohru Saitoh, and Masakazu Yoshida for technical support.

References

1. Marmor MF, Aguirre G, Arden G, et al. Retinitis pigmentosa: a symposium on terminology and methods of examination. *Ophthalmology.* 1983;90:126–131.
2. Pagon RA. Retinitis pigmentosa. *Surv Ophthalmol.* 1988;33:137–177.
3. Margalit E, Maia M, Weiland JD, et al. Retinal prosthesis for the blind. *Surv Ophthalmol.* 2002;47:335–356.